J. Fluid Mech. (2021), *vol.* 919, A19, doi:10.1017/jfm.2021.415

Vortical–acoustic resonance in an acoustic resonator: Strouhal number variation, destabilization and stabilization

Xiwen Dai†

School of Mechanical Engineering, Shanghai Jiao Tong University, Shanghai 200240, PR China

(Received 23 November 2020; revised 29 March 2021; accepted 3 May 2021)

The impact of acoustic resonance on vortical–acoustic resonance and flow instability is studied by a combined travelling–global mode analysis about a low-speed inviscid parallel shear flow in two-dimensional symmetric duct–cavity configurations. First, in a shallow-cavity case, we show that the difference between incompressible and compressible models in describing the compact feedback loop, consisting of the Kelvin–Helmholtz (KH) instability wave and the Rayleigh–Powell–Rossiter (RPR) feedback, is small and the global mode frequency follows the Strouhal law. Using the compact case as a baseline for comparison, the influence of an acoustic resonator (AR) on the KH + RPR feedback loop is then examined. In this deep-cavity case, phenomena such as frequency deviation from the Strouhal law, global mode switching, global mode destabilization and stabilization, caused by a trapped or a heavily damped acoustic resonant mode, are observed. We show that those phenomena can be explained by the local–global relation of the feedback loop and the dual-feedback view: the coexistence of RPR and AR feedbacks. The Strouhal number variation is due to the phase difference of the unstable vortical wave between the upstream and downstream cavity edges being changed by the additional AR feedback. It is found that the switching is not a vortical but an acoustic effect. The destabilization and stabilization, near and far from an acoustic resonance, are respectively understood as the result of the total feedback at the upstream edge being strengthened and weakened by the AR feedback.

Key words: aeroacoustics, shear-flow instability

1. Introduction

Flow tones generated by shear layers interacting with solid surfaces have been studied for decades, however, investigating these problems can still provide a substantial advance in our understanding of vortical–acoustic interaction. With a shear flow past an open

---

† Email address for correspondence: xiwen.dai@sjtu.edu.cn

cavity, self-sustained oscillations can happen owing to the feedback-loop mechanism that is usually attributed to Rossiter (1964): the spatially growing Kelvin–Helmholtz (KH) instability wave scatters into acoustic waves at the downstream edge, and acoustic waves propagate upstream and excite the new instability wave. Rossiter also obtained a semi-empirical formula for oscillation frequencies based on the phase relation of the feedback loop. Essentially the same feedback-loop mechanism was known earlier in jet edge tones (Powell 1953, 1961). Powell has examined not only the loop phase relation, but also the loop gain (the loop amplitude relation) which is relevant to whether self-sustained oscillations happen or not at the frequencies determined by the phase requirement. The original feedback-loop idea has been credited to Lord Rayleigh (see Powell 1995), who described the mechanism of a high-pitched whistle called a bird call (Rayleigh 1945). Over the past decades, such a feedback-loop mechanism has been found to be responsible for many tonal flows, such as cavity flows and impinging jets (see reviews such as Rockwell & Naudascher (1978), Blake & Powell (1986), Fabre & Hirschberg (2000), Rowley & Williams (2006), Gloerfelt (2009), Tonon *et al.* (2011), Edgington-Mitchell (2019)).

In a cavity flow, the free shear layer spanning the cavity is perturbed by the feedback acoustic disturbances (Ho & Huerre 1984). At low Mach numbers, the acoustic excitation is only effective near the separation point where vortical disturbances are generated, owing to the mismatch between the wavelengths of acoustic and instability waves. The later vortical motions between the separation point and the downstream solid surface, which may appear as spatially growing instability waves in some cases or as concentrated vortex structures in others, largely depend on the initial acoustic excitation (Bauerheim, Boujo & Noiray 2020).

The upstream feedback is not limited to acoustic waves that are associated with the compressibility of fluids, it can be truly hydrodynamic. Incompressible cavity flow oscillations have been observed in experiments, which show similar feedback-loop features as described in the Rossiter model (Knisely & Rockwell 1982; Gharib & Roshko 1987). The existence of purely hydrodynamic resonances has been confirmed by incompressible global mode calculations (Barbagallo, Sipp & Schmid 2009; Yamouni, Sipp & Jacquin 2013). At very low Mach numbers, the whole self-sustained system is in the very near field, i.e. the configuration is small compared with the acoustic wavelength (acoustically compact), a hydrodynamic description is also applicable (Powell 1961; Ffowcs-Williams 1969; Crighton 1992; Howe 1997). In this regime, the upstream feedback might be designated as pseudo-sound (Ffowcs-Williams 1969). Following Goldstein (1978), the irrotational feedback disturbances are still referred to as acoustic in this article even though they can be supported by an incompressible model. The designation 'acoustic' distinguishes those irrotational disturbances from vortical disturbances that are associated with flow shear. In incompressible or compact cases, since the phase relation of the feedback loop is mainly determined by the vortical motions in the shear layers, the oscillation frequency is roughly proportional to the flow velocity, following the Strouhal law.

The feedback loop consisting of KH instability waves and the Rayleigh–Powell–Rossiter (RPR) feedback can be dramatically influenced by an acoustic resonant mode of the cavity, the Rossiter formula then fails to predict oscillation frequencies (East 1966; Tam & Block 1978). Experimental results of such an influence were typically obtained at low flow speeds, and the oscillation frequencies have been shown to deviate from the expected Strouhal law (Nelson, Halliwell & Doak 1981; Bruggeman *et al.* 1991; Kook & Mongeau 2002; Ma, Slaboch & Morris 2009; Dai, Jing & Sun 2015). In some cases, it appears that the resonator almost completely imposes its resonant frequencies on the whole self-sustained system (Ziada & Shine 1992; Peters 1993; Kriesels *et al.* 1995; Tonon *et al.* 2011), which is often referred to as frequency lock in. The influence of the resonator also leads to intense self-sustained oscillations and concentrated vortex structures. Similar phenomena happen in many other configurations, such as a flow duct containing plates (Parker 1966; Stoneman *et al.* 1988) and a compressor (Hellmich & Seume 2008), leading to an extensive study of acoustic resonance without flow in open systems (Hein, Hohage & Koch 2004; Koch 2009; Hein, Koch & Nannen 2012).

The flow-tone problem sketched in figure 1 is considered in this article. Two types of approaches can be used in studying the self-sustained flow oscillations, where shear flows are respectively described as vorticity fields in physical space and hydrodynamic instability waves in Fourier space (Ho & Huerre 1984). The first approach, such as using the vortex particle method to model shear layer motions (Peters 1993; Kriesels *et al.* 1995; Dai *et al.* 2015), gives the nonlinear evolution of the shear layers, which can be compared with flow-visualization studies. In the second approach, the examination of the linear tonal dynamics of shear flows is achieved by global mode analyses (Sipp *et al.* 2010; Theofilis 2011; Yamouni *et al.* 2013; Fosas de Pando, Schmid & Sipp 2014). It is very often that global modes need to be numerically solved from global eigenvalue problems when solid surfaces and mean flows are complex. For a complete understanding of vortical–acoustic coupling and global instabilities here, a combined local–global analysis with a simplified flow model (Gallaire & Chomaz 2004; Doaré & de Langre 2006; Stewart, Waters & Jensen 2009) is also desirable. Thus, the present global modes are constructed from travelling vortical and acoustic waves by the feedback-loop closure principle (Landau & Lifshitz 1981) described in § 2, under the assumption of a parallel mean flow. Such a closure principle reflects the idea of Rayleigh, Powell and Rossiter for global instabilities and the consequent self-sustained oscillations, and it embraces cases whether or not a resonator is present (Powell 1990).

The main objective of this article is to examine the influence of an acoustic resonator (AR) on the KH + RPR feedback loop. It has been shown that a linear global mode analysis can predict interesting phenomena and provide insight into the influence of an AR on global instabilities and self-sustained oscillations (Alvarez & Kerschen 2005; Méry 2010; Yamouni *et al.* 2013). For example, an overshoot in temporal growth rate and a global mode switching happen near the frequency of some acoustic resonant modes (Yamouni *et al.* 2013). For a better understanding of the global mode-related phenomena, a combined travelling–global mode analysis is performed in the present study, taking full advantage of the feedback-loop closure principle. The research plan is as follows. First, the compact case sketched in figure 1(*a*) is considered in § 3.1, serving as a baseline for comparison. It is noted that a compact case was analysed in Dai (2020), with a compressible model. Here, a purely hydrodynamic feedback loop supported by an incompressible model is demonstrated and compared with the compressible results. Then, two acoustic resonant modes for the deep-cavity case in figure 1(*b*) but without flow are calculated in § 3.2. The antisymmetric one is a trapped mode which is decoupled from the outgoing propagative travelling modes in the ducts, corresponding to an acoustic resonance with a high quality factor (Pagneux 2013). The symmetric one is a heavily damped mode owing to radiation. Finally, the vortical–acoustic resonance sketched in figure 1(*b*) is discussed in § 3.3. Different impacts of the trapped and heavily damped acoustic modes on the global modes are shown. Phenomena such as frequency deviation from the Strouhal law, global mode switching, global mode destabilization and stabilization are explained by the local–global relation of the feedback loop and the dual-feedback view (Powell 1990; Fabre & Hirschberg 2000; Rienstra & Hirschberg 2018): the coexistence of RPR and

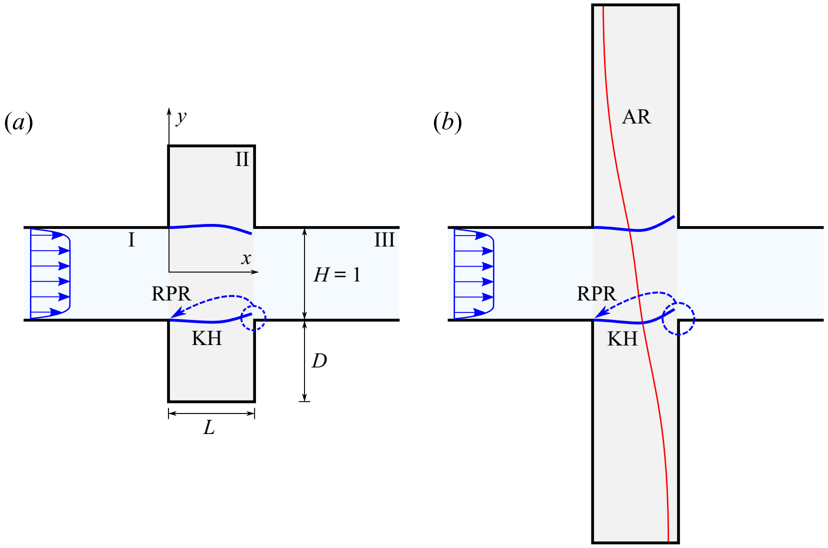

Figure 1. Sketches of vortical–acoustic resonance at low flow speeds in two-dimensional (2-D) symmetric duct–cavity configurations, where the flow duct is infinitely long. (*a*) A shallow-cavity case with a compact KH + RPR feedback loop, (*b*) a deep-cavity case where the compact KH + RPR feedback loop is affected by the resonator acoustics. The symmetric and antisymmetric (breathing and flapping) KH modes of the jet profile (Tam & Norum 1992; Gojon, Bogey & Marsden 2016; Martini, Cavalieri & Jordan 2019) in the cavity segment are respectively sketched in (*a*) and (*b*).

AR feedbacks. Note that antisymmetric and symmetric respectively denote y-antisymmetric and y-symmetric in this article.

2. Numerical model

Calculations of vortical–acoustic resonant modes (also called global modes) and acoustic resonant modes are rather simple here. The global mode calculation has been described in Dai (2020) for a compact case, and it is outlined in this section. The duct–cavity configuration is divided into three zones, as shown in figure 1(*a*): the left semi-infinite duct (zone I), the cavity segment (zone II) and the right semi-infinite duct (zone III). In each zone, duct modes travelling in the $\pm x$ directions are first solved (Kooijman *et al.* 2008; Kooijman, Hirschberg & Aurégan 2010). The resonant modes are then constructed from the travelling duct modes by the feedback-loop closure principle between the two ends of the cavity segment.

2.1. *Governing equations and calculations of travelling duct modes*

The linear propagation of vortical and acoustic disturbances in each zone about a parallel mean shear flow is described by the linearized Euler equations (LEEs)

$$\left(\frac{\partial}{\partial t}+M_0 f\frac{\partial}{\partial x}\right)u+M_0\frac{\mathrm{d}f}{\mathrm{d}y}v=-\frac{\partial p}{\partial x}, \tag{2.1}$$

$$\left(\frac{\partial}{\partial t}+M_0 f\frac{\partial}{\partial x}\right)v=-\frac{\partial p}{\partial y}, \tag{2.2}$$

$$\left(\frac{\partial}{\partial t}+M_0 f\frac{\partial}{\partial x}\right)p=-\left(\frac{\partial u}{\partial x}+\frac{\partial v}{\partial y}\right), \tag{2.3}$$

where u and v are the velocity disturbance in respectively the x- and y-directions, p is the pressure disturbance, M_0 is the average Mach number in the duct with the profile prescribed by the function $f(y)=M(y)/M_0$ (the assumed velocity profile of the low-speed mean flow is described at the beginning of § 3.1) and all variables have been normalized by sound speed c_0^* and density ρ_0^* and the duct height H^*. The stars in this article denote dimensional quantities, whereas quantities without star are dimensionless.

The fluctuations are sought in the form

$$\left.\begin{aligned} p&=P(y)\exp(-\mathrm{i}kx)\exp(\mathrm{i}\omega t),\\ v&=V(y)\exp(-\mathrm{i}kx)\exp(\mathrm{i}\omega t),\end{aligned}\right\} \tag{2.4}$$

where $\mathrm{i}^2=-1$, k is the wavenumber and ω is the angular frequency. Inserting (2.4) into the LEEs leads to

$$\mathrm{i}(\omega-M_0 fk)V=-\frac{\mathrm{d}P}{\mathrm{d}y}, \tag{2.5}$$

$$\left(1-M_0^2f^2\right)k^2P+2\omega M_0 fkP-\omega^2P-\frac{\mathrm{d}^2P}{\mathrm{d}y^2}=-2\mathrm{i}M_0\frac{\mathrm{d}f}{\mathrm{d}y}kV. \tag{2.6}$$

In each zone, vortical and acoustic travelling modes are solved by discretizing (2.5) and (2.6) in the y-direction, taking N_1 equally spaced points in zones I and III, N_2 equally spaced points in zone II. The spacing between interior points in all zones is $\Delta h=H/N_1=(2D+H)/N_2$, and the first and last points are taken $\Delta h/2$ from the solid walls. Equations (2.5) and (2.6), together with the wall boundary conditions, determine the following generalized eigenvalue problem in each zone:

$$k\begin{pmatrix} \boldsymbol{I}-M_0^2\boldsymbol{f}_2 & 2\mathrm{i}M_0\boldsymbol{f}_a & \boldsymbol{0}\\ \boldsymbol{0} & \mathrm{i}M_0\boldsymbol{f} & \boldsymbol{0}\\ \boldsymbol{0} & \boldsymbol{0} & \boldsymbol{I}\end{pmatrix}\begin{pmatrix}\boldsymbol{Q}\\ \boldsymbol{V}\\ \boldsymbol{P}\end{pmatrix}=\begin{pmatrix} -2\omega M_0\boldsymbol{f} & \boldsymbol{0} & \omega^2\boldsymbol{I}+\boldsymbol{D}_2\\ \boldsymbol{0} & \mathrm{i}\omega\boldsymbol{I} & \boldsymbol{D}_1\\ \boldsymbol{I} & \boldsymbol{0} & \boldsymbol{0}\end{pmatrix}\begin{pmatrix}\boldsymbol{Q}\\ \boldsymbol{V}\\ \boldsymbol{P}\end{pmatrix}, \tag{2.7}$$

where $Q=kP$ is assumed, $\boldsymbol{I}$ is the identity matrix, $\boldsymbol{f}$, $\boldsymbol{f}_2$ and $\boldsymbol{f}_a$ are diagonal matrices with on the diagonal the values of f, f^2 and $\mathrm{d}f/\mathrm{d}y$ at the discrete points; $\boldsymbol{Q}$, $\boldsymbol{V}$ and $\boldsymbol{P}$ are the column vectors giving respectively the value of $Q(y)$, $V(y)$ and $P(y)$ at the discrete points; $\boldsymbol{D}_1$ and $\boldsymbol{D}_2$ are matrices for the first- and second-order differential operators with respect to y. The boundary condition $\mathrm{d}p/\mathrm{d}y=0$ on the solid walls is taken into account in the differential operator matrices by introducing ghost points outside the walls. The eigenvalue problems for the duct modes are then solved, using the `eig` function of MATLAB. In zones I and III, $3N_1$ modes are obtained, including N_1 acoustic modes travelling in the $\pm x$ directions and N_1 vortical modes travelling in the $+x$ direction with the mean flow. In zone II, the mean flow velocity and its derivative are zero at discrete points where $|y|>H/2$. The first and last $(N_2-N_1)/2$ rows and columns of the middle parts in the matrices in (2.7) and the first and last $(N_2-N_1)/2$ elements of $\boldsymbol{V}$ are skipped, corresponding to the no-flow parts of this zone. Thus, N_2 acoustic modes travelling in the $\pm x$ directions and N_1 vortical modes travelling in the $+x$ direction are solved in zone II.

For the compact configuration shown in figure 1(*a*), global modes will also be calculated with an incompressible model and compared with results from the LEEs. The incompressible equivalent to (2.6) is

$$k^2 P - \frac{\mathrm{d}^2 P}{\mathrm{d}y^2} = -2\mathrm{i}M_0 \frac{\mathrm{d}f}{\mathrm{d}y} kV. \tag{2.8}$$

Note that, in the incompressible model, the velocity used in the normalization is still the sound speed of the compressible problem, which leads to the appearance of M_0 in the normalized equations (Marx & Aurégan 2013). This choice of normalization will allow a direct comparison between the incompressible and compressible global modes in the compact case. In each zone, solving the eigenvalue problems by the same discretization of (2.5) and (2.8) in the y-direction as of (2.5) and (2.6) leads to the same numbers of vortical and 'acoustic' travelling modes as those vortical and acoustic travelling modes solved from the LEEs. However, these vortical and 'acoustic' modes solved from (2.5) and (2.8) are both purely hydrodynamic.

Acoustic resonant modes without flow, of the configuration shown in figure 1(*b*), will be calculated. Without flow, the governing equation of acoustic disturbances is a wave equation

$$\frac{\partial^2 p}{\partial t^2} - \left(\frac{\partial^2 p}{\partial x^2} + \frac{\partial^2 p}{\partial y^2}\right) = 0. \tag{2.9}$$

Inserting (2.4) into (2.9) leads to

$$k^2 P - \omega^2 P - \frac{\mathrm{d}^2 P}{\mathrm{d}y^2} = 0. \tag{2.10}$$

In each zone, after introducing $Q = kP$, solving the eigenvalue problems with the same grid points in the y direction as used in solving the eigenvalue problems above leads to the same number of acoustic travelling modes as those solved from the LEEs.

2.2. *Calculations of acoustic and vortical–acoustic resonant modes*

Acoustic and vortical–acoustic resonant modes can be numerically solved from global eigenvalue problems in a large enough domain with boundary conditions that only allow outgoing waves (Hein *et al.* 2004; Sipp *et al.* 2010; Theofilis 2011). This approach applies to complex solid boundaries and mean flows.

Under the assumption of a segmented homogeneous system, resonant modes can also be easily constructed from the travelling modes in the segments by the feedback-loop closure principle. Each resonant mode is assembled by the $\pm x$ travelling modes that, around a feedback loop including wave propagation and wave reflection, have the same amplitude while the phase change is an integral multiple of 2π at a complex or real-valued resonance frequency (Landau & Lifshitz 1981). The closure principle has been widely used in investigating global instabilities and resonances (Doaré 2001; Gallaire & Chomaz 2004; Alvarez, Kerschen & Tumin 2004; Doaré & de Langre 2006; Stewart *et al.* 2009; de Lasson *et al.* 2014; Tuerke *et al.* 2015; Jordan *et al.* 2018).

A most simple example for the loop closure principle is that each normal mode in an infinite 2-D waveguide means a resonance in the transverse direction (Jensen *et al.* 2011), and the closure principle is satisfied in that direction. Vortical and acoustic duct modes solved in § 2.1 satisfy the resonant condition in the transverse direction. To construct a system resonant mode in the 2-D duct–cavity configurations, one then needs to determine the particular complex frequency and the particular combination of those duct modes so that the resonant condition in the longitudinal direction is satisfied. To this end, a multimodal feedback-loop matrix can be defined, $\boldsymbol{M}_{fl} = \boldsymbol{R}_u \boldsymbol{P}_u \boldsymbol{R}_d \boldsymbol{P}_d$. Using the compressible model associated with the LEEs for example, $\boldsymbol{R}_u$ $((N_2 + N_1) \times N_2)$ and $\boldsymbol{R}_d$ $(N_2 \times (N_2 + N_1))$ are respectively the upstream and downstream reflection matrices for the $\mp x$ travelling modes in the cavity segment, describing wave reflection at the segment ends; $\boldsymbol{R}_u$ (respectively $\boldsymbol{R}_d$) is extracted from the interface scattering matrix at the upstream (respectively downstream) end of the cavity segment which is calculated by matching the travelling modes in the cavity segment and the travelling modes in the upstream (respectively downstream) duct; $\boldsymbol{P}_u$ $(N_2 \times N_2)$ and $\boldsymbol{P}_d$ $((N_2 + N_1) \times (N_2 + N_1))$ are respectively the upstream and downstream propagation matrices, describing wave travelling inside the cavity segment; $\boldsymbol{P}_u$ and $\boldsymbol{P}_d$ are diagonal matrices with the elements on the diagonal being $\exp(\pm \mathrm{i} k_n^{\mp} L)$, where $k_n^{\mp}$ are respectively the wavenumbers of the nth upstream- and downstream-travelling modes. The upstream-travelling waves are only acoustic waves, while the downstream-travelling waves include acoustic and vortical waves. Note that $\boldsymbol{P}_{u,d}$ and $\boldsymbol{R}_{u,d}$ are also called propagation and reflection links of the feedback loop. In § 3, we focus on analysing $\boldsymbol{P}_{u,d}$, although $\boldsymbol{R}_{u,d}$ can also be significant to the global instabilities of a system (Gallaire & Chomaz 2004; Doaré & de Langre 2006). In the incompressible model, the dimensions of the matrices are the same as those in the compressible model. In the calculations of acoustic resonant modes without flow, the travelling modes are only acoustic modes and the dimensions of the matrices accordingly change. The loop closure principle means that one of the eigenvalues of $\boldsymbol{M}_{fl}$ is unity at the complex frequency of a resonant mode: $\boldsymbol{M}_{fl} \boldsymbol{C}_{fl} = k_{fl} \boldsymbol{C}_{fl}$ with $k_{fl} = 1$. In the resonant mode calculations, the complex frequency ω is optimized (using the `fminsearch` function of MATLAB), so that one of the eigenvalues of $\boldsymbol{M}_{fl}$ is equal to unity. The corresponding eigenvector, $\boldsymbol{C}_{fl}$, contains the coefficients of the travelling modes that lead to the spatial distribution of a resonant mode, which is also an eigenfunction of the global eigenvalue problem (Hein *et al.* 2004; Sipp *et al.* 2010; Theofilis 2011). The iteration stops when the error between the target k_{fl} and unity is less than $E_o = 10^{-10}$. Here, $N_1 = 400$ and $N_2 = N_1(2D + H)/H$ is used in the calculations and a convergence assessment is given in Appendix A.

As noted in Dai (2020), the terms global mode and global instability are used in the sense that 'since this instability is due to the properties of the system as a whole, it is called global instability' (Landau & Lifshitz 1981). It is also very often that 'the term global is used to distinguish the analysis from the classic local linear stability theory, where the base flow is independent of two coordinate directions' (Taira *et al.* 2017).

3. Results

3.1. *Hydrodynamic resonance in an acoustically compact configuration*

Vortical–acoustic resonance in the compact configuration sketched in figure 1(*a*), that is, the cavities are small compared with the acoustic wavelength (Nakiboglu *et al.* 2011; Nakiboglu, Manders & Hirschberg 2012; Dai 2020), is calculated with the compressible and incompressible models in this subsection. The geometrical parameters are $H^* = 50$ mm, $D^* = 25$ mm and $L^* = 25$ mm. The Mach number averaged over the cross-section of the flow duct varies over the range 0.03 to 0.15, and the velocity profile is prescribed by $f = (1 - (2y)^m)(m + 1)/m$, where the parameter $m = 8$ is used. The mean flow is assumed unchanged along the entire duct–cavity configuration, which means that a jet velocity profile is formed and the mean velocity is zero at $|y| > H/2$ in the cavity segment.

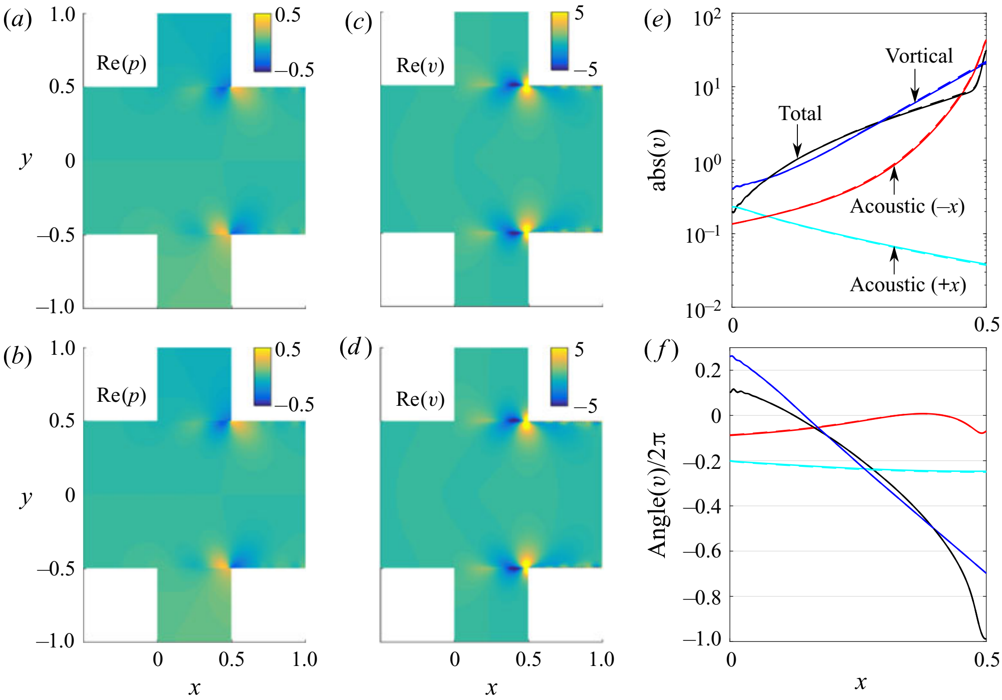

Figure 2. Spatial distribution of the antisymmetric global mode for $M_0 = 0.09$ calculated from the compressible ((*a*,*c*), where $\omega_G = 0.4054 + 0.0036\mathrm{i}$) and incompressible ((*b*,*d*), where $\omega_G = 0.4055 + 0.0046\mathrm{i}$) models. Amplitude (*e*) and phase (*f*) of v along the opening of the low cavity (at the point just below $y = -H/2$). Solid lines, compressible model; dashed lines, incompressible model.

The discontinuity in $\mathrm{d}f/\mathrm{d}y$ at $y = \pm H/2$ in the cavity segment causes a convergence problem in solving the travelling modes, and inflexion points are not defined at $y = \pm H/2$. By empirically introducing a resistive sheet with a small resistance $R = 0.2M_0$ at $y = \pm H/2$ (Dai & Aurégan 2018; Dai 2020), the convergence problem is mitigated and the instability characteristics of the shear flow are similar to those of a hyperbolic–tangent velocity profile (Michalke 1965; Schmid & Henningson 2001). The resistive sheets result in a pressure jump $\Delta p = Rv$ at $y = \pm H/2$ in the cavity segment. It is noted that this choice of the mean flow model leads to a piecewise homogeneous problem, so that the travelling mode analysis is rather simple, and to the continuity of the mean velocity between the cavity and duct segments, so that the disturbances are continuous at the interfaces between segments when mass and momentum conservation are enforced.

The spatial distributions of the antisymmetric and symmetric global modes for $M_0 = 0.09$ are presented in figures 2(*a*–*d*) and 3(*a*–*d*), where the fields have been normalized by v at $x = L/4$ and $y = -H/2$. As expected, for an acoustically compact problem, the spatial distributions calculated from the compressible and incompressible models are almost exactly the same. A compact global mode here is mainly formed by a downstream-travelling unstable vortical mode (the antisymmetric or symmetric KH mode) and multiple upstream-travelling acoustic modes. The primary analysis approach is to first separate the travelling modes into three groups, namely vortical and ±x acoustic, then seeing the spatial variation of disturbances of each group. An analysis of the multiple feedback-loop channels is given in Appendix B. The modal shape of the global modes indicates that strong oscillations are concentrated in the opening area of the cavities, thus

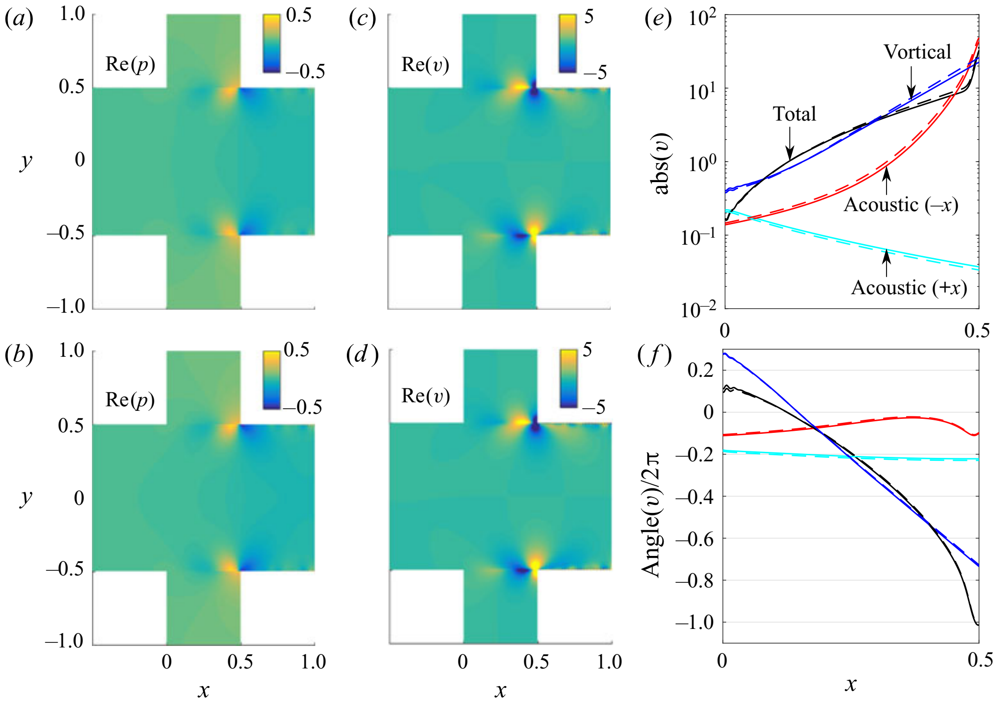

Figure 3. Spatial distribution of the symmetric global mode for $M_0 = 0.09$ calculated from the compressible ((*a*,*c*), where $\omega_G = 0.4126 + 0.0051\mathrm{i}$) and incompressible ((*b*,*d*), where $\omega_G = 0.4114 + 0.0089\mathrm{i}$) models. For the descriptions of (*e*,*f*), see figure 2.

an approximate way to examine the propagation link ($\boldsymbol{P}_u$ and $\boldsymbol{P}_d$) of the feedback loop is to see the variation of v along the line between the two edges of the upper or lower cavity, as shown in figures 2(*e*,*f*) and 3(*e*,*f*). Around the feedback loop, the phase change associated with the RPR upstream feedback is small and the phase change of the KH modes is close to 2π, which agree with the previous understanding of the Rossiter modes in compact cases.

The global mode frequency ω_G as a function of M_0 is presented in figure 4. It is shown that $\mathrm{Re}(\omega_G)$ follows the Strouhal law ($Sr = \mathrm{Re}(\omega)L/2\pi M_0$), which is in line with the previous experiments of incompressible or acoustically compact cavity flow oscillations (Knisely & Rockwell 1982; Gharib & Roshko 1987; Nakiboglu *et al.* 2011, 2012). Note that the spatial distributions at the other Mach numbers in figure 4 are all similar to those shown in figures 2 and 3 for $M_0 = 0.09$. The phase difference of the KH modes between the upstream and downstream edges is almost constant and close to 2π for all these Mach numbers, which explains the Strouhal law and also the coincidence between the compressible and incompressible results of Sr.

The temporal growth rate of the global modes, $-\mathrm{Im}(\omega_G)$ according to the $\exp(\mathrm{i}\omega t)$ convention, in figure 4(*b*) shows the increasing discrepancy between the compressible and incompressible models as M_0 is increased. The value of $\mathrm{Im}(\omega_G)$ calculated from the incompressible model shows a linear increase with M_0. This is because the incompressible global modes calculated with different M_0 actually describe the same hydrodynamic feedback loop, which is indicated by the constant Sr in figure 4(*a*) and the wavenumbers shown in figure 5(*b*). The wavenumbers calculated from the incompressible model overlap for the seven M_0 and the corresponding $\mathrm{Re}(\omega_G)$. For the seven M_0 and the corresponding ω_G, the wavenumbers shift from those calculated with real-valued frequencies, but they

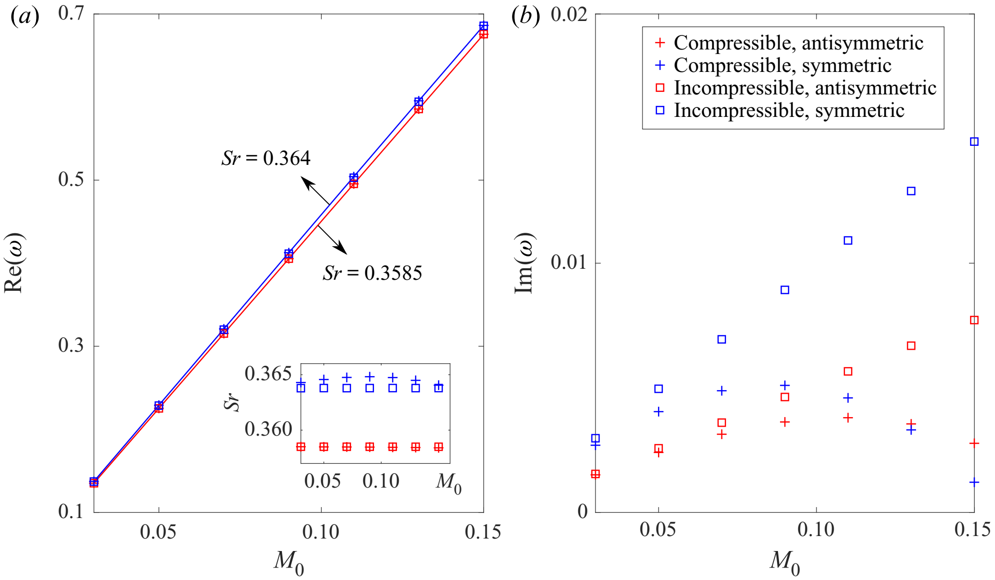

Figure 4. Global mode frequency as a function of M_0 in the compact case, calculated from the compressible and incompressible models. The legend in (*b*) also applies to (*a*).

still overlap. The latter overlap requires $\mathrm{Im}(\omega_G)$ being proportional to $\mathrm{Re}(\omega_G)$, and being proportional to M_0. On the other hand, figure 5(*a*) shows that the wavenumbers from the compressible model vary with M_0 and the KH modes show the stabilization effect of the Mach number on the KH convective instability (Miles 1958). Although the wavenumbers only represent the propagation link ($\boldsymbol{P}_u$ and $\boldsymbol{P}_d$) of the feedback loop, the deviations of the compressible results of the wavenumbers and $\mathrm{Im}(\omega_G)$ from their incompressible counterparts show the same trend with increasing M_0. It is noted that the compressible and incompressible wavenumbers in a lined flow duct have also been shown to be close to each other at a low Mach number but are not exactly the same (Marx & Aurégan 2013). It is also noted that, for the present parameters, figure 4(*b*) shows a stable KH + RPR feedback loop, which can be destabilized by reducing the shear layer thickness (Yamouni *et al.* 2013) or reducing R (Dai 2020), as discussed below.

The feedback-loop closure principle ($k_{fl} = 1$) implies two conditions of a system resonant mode: the phase condition ($\arg(k_{fl}) = 2j\pi$, where j is an integer) and the gain or amplitude condition ($|k_{fl}| = 1$). The real part of the global mode frequency $\mathrm{Re}(\omega_G)$ is mainly decided by the phase condition, whereas the temporal growth rate $\mathrm{Im}(\omega_G)$ is associated with the amplitude condition. For each global mode, no matter whether the mode is globally stable, neutral or unstable, both $\arg(k_{fl}) = 2j\pi$ and $|k_{fl}| = 1$ should be satisfied at the global mode frequency ω_G. For stable, neutral and unstable global modes, the loop gain at $\mathrm{Re}(\omega_G)$ is respectively $|k_{fl}| < 1$, $|k_{fl}| = 1$ and $|k_{fl}| > 1$. Therefore, a loop-gain criterion of global instability can be obtained: $|k_{fl}|$ being larger or smaller than unity at $\mathrm{Re}(\omega_G)$ determines whether the global mode is unstable or stable (Alvarez & Kerschen 2005; Rowley *et al.* 2006; Dai 2020). Note that the above loop-gain criterion of global instability is slightly different from Powell's gain condition, i.e. a unit gain at a real frequency, which was used to describe the saturated and stable state of self-sustained oscillations (Powell 1961). To better understand the above discussions, the eigenvalues of $\boldsymbol{M}_{fl}$ and the wavenumbers of the travelling modes in the cavity segment are plotted in

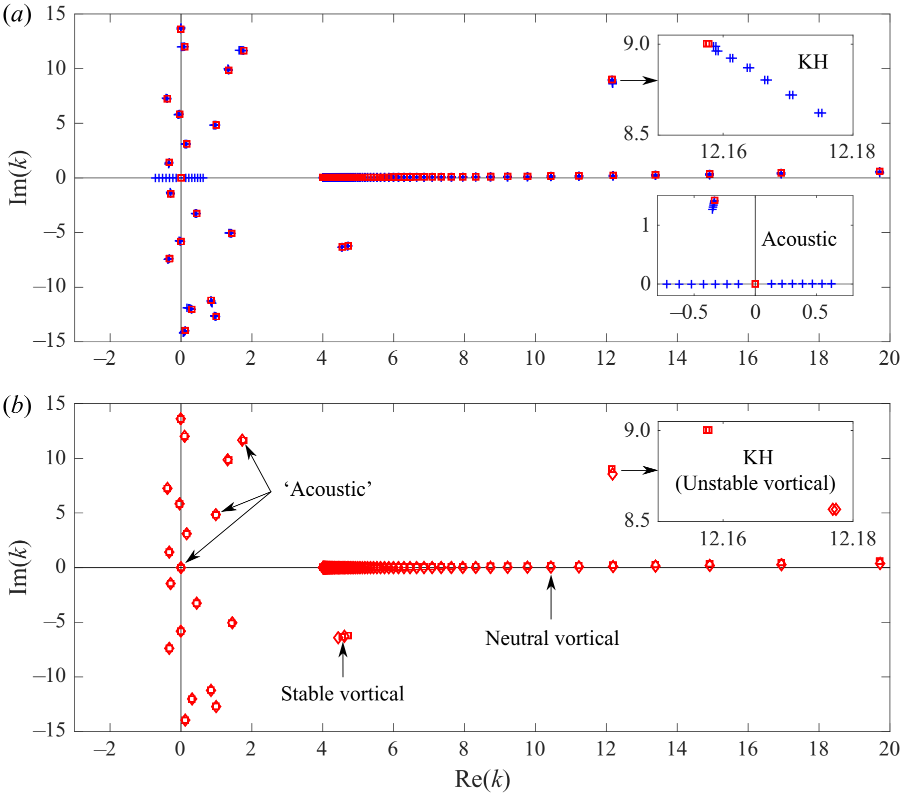

Figure 5. (*a*) Wavenumbers in the cavity segment calculated from the compressible (crosses) and incompressible (squares) models with M_0 and ω_G of the antisymmetric modes in figure 4; (*b*) wavenumbers in the cavity segment calculated from the incompressible model with M_0, ω_G (squares) and $\mathrm{Re}(\omega_G)$ (diamonds) of the antisymmetric modes in figure 4.

figure 6, as the complex frequency is perturbed from ω_G. It is shown that, at ω_G for the antisymmetric global mode, one eigenvalue of $\boldsymbol{M}_{fl}$ is unity. Another eigenvalue of $\boldsymbol{M}_{fl}$, close to unity, is associated with the symmetric global mode, whose feedback loop is not closed yet. Note that the global modes with multiple KH wavelengths in the cavity opening region (Nakiboglu *et al.* 2011, 2012; Yamouni *et al.* 2013) are damped here, because the shear layers are rather thick. First, the variation of $\mathrm{Re}(\omega)$ leads to k_{fl} rotating around zero in the complex plane (the trajectory of a k_{fl} is not exactly a circle, however) as shown in figure 6(*a*), since the wavelengths of the travelling modes change with $\mathrm{Re}(\omega)$ as shown in figure 6(*b*). This demonstrates how the multiple Rossiter frequencies are selected by the loop phase condition: $\arg(k_{fl}) = 2j\pi$, where j is an integer. Second, the variation of $\mathrm{Im}(\omega)$ leads to the change of $|k_{fl}|$, since the spatial growth rate ($\pm\mathrm{Im}(k)$ respectively for the waves travelling in the $\pm x$ directions) of the travelling vortical and acoustic modes, being positive or negative, varies with $\mathrm{Im}(\omega)$. It has been revealed that, in general, a thinner shear layer potentially results in stronger self-sustained oscillations in cavity flows (Knisely & Rockwell 1982; Gharib & Roshko 1987; Nakiboglu *et al.* 2012). The stronger self-sustained oscillations of a fully nonlinear flow system are understood to be associated with the stronger global instabilities, i.e. larger $-\mathrm{Im}(\omega_G)$ (Yamouni *et al.* 2013). It was also known that reducing the shear layer thickness leads to a larger spatial growth rate of the KH instability waves (Schmid & Henningson 2001). Figure 6 casts light on the link

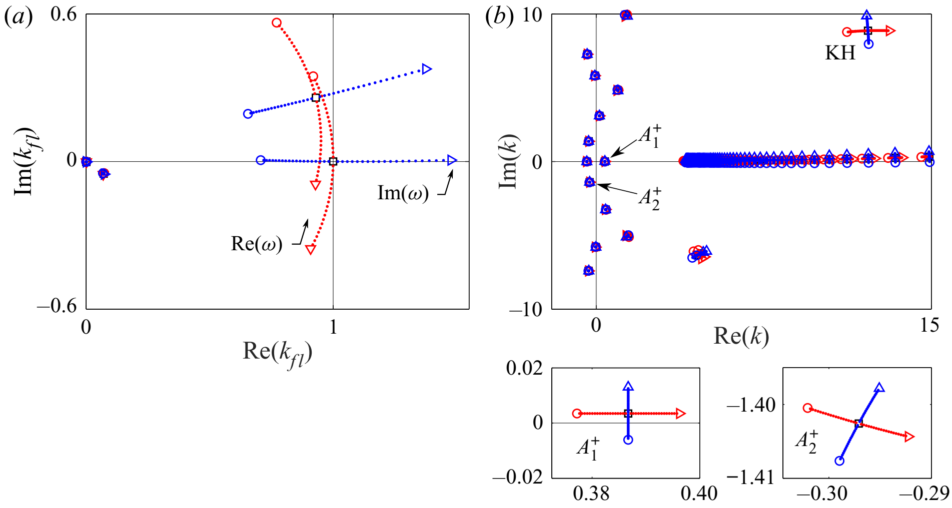

Figure 6. Variations of (*a*) the eigenvalues of $\boldsymbol{M}_{fl}$ and (*b*) the wavenumbers in the cavity segment as the frequency is perturbed from $\omega_G = 0.4054 + 0.0036\text{i}$ (the antisymmetric global mode frequency for $M_0 = 0.09$ calculated with the compressible model). Red, $\text{Re}(\omega)$ varying from $\text{Re}(\omega_G) - 0.01$ (circles) to $\text{Re}(\omega_G) + 0.01$ (triangles); blue, $\text{Im}(\omega)$ varying from $\text{Im}(\omega_G) - 0.01$ (circles) to $\text{Im}(\omega_G) + 0.01$ (triangles).

between the increase in the spatial growth rate of travelling waves and flow destabilization. The former would cause an increase of $|k_{fl}|$ if $\text{Im}(\omega)$ remains unchanged. To maintain the $k_{fl} = 1$ condition for a resonant mode, $\text{Im}(\omega)$ should decrease, that is, a global mode destabilization. It is noted that, in the above local–global analysis of the feedback loop, both frequency and wavenumber can be complex and a real-valued frequency is not more special than a complex frequency (Gallaire & Chomaz 2004; Doaré & de Langre 2006; Stewart *et al.* 2009; Jordan *et al.* 2018), thus $\text{Im}(\omega_G)$ decreasing or increasing, rather than ω_G crossing the real axis, is referred to as global mode destabilization or stabilization in this article. Such a local–global relation of the feedback loop applies to both acoustic and vortical–acoustic resonances.

3.2. *Acoustic resonator*

To study the influence of an AR on the KH + RPR feedback loop, the depth of the cavities will be increased, $D^* = 200$ mm ($D/L = 8$), whereas all the other geometrical and flow parameters remain the same as those in § 3.1. Before discussing the vortical–acoustic resonance in an AR in § 3.3, we first examine the resonator acoustics without flow. Acoustic resonant modes in cavities have been studied by Tam (1976), Koch (2005), Hein *et al.* (2012) and others, here, only the modes needed for the later discussions are calculated. The first antisymmetric and symmetric acoustic resonant modes are respectively presented in figures 7 and 8, where the modes are normalized so that $|p| = 1$ at the cavity bottoms.

The antisymmetric acoustic resonant mode displayed in figure 7(*a–c*) is a trapped mode. The coefficients of the $+x$ travelling modes in the cavity segment (at $x = 0$) and in the right duct (at $x = L$) are shown in figure 7(*e*), where the travelling modes have been normalized so that $|P_n(y)|_{max} = 1$. Note that the coefficient of the nth $-x$ travelling mode in the cavity segment (at $x = L$) or in the left duct (at $x = 0$), which is not shown, is exactly the same as that of the nth $+x$ travelling mode. The split between symmetric

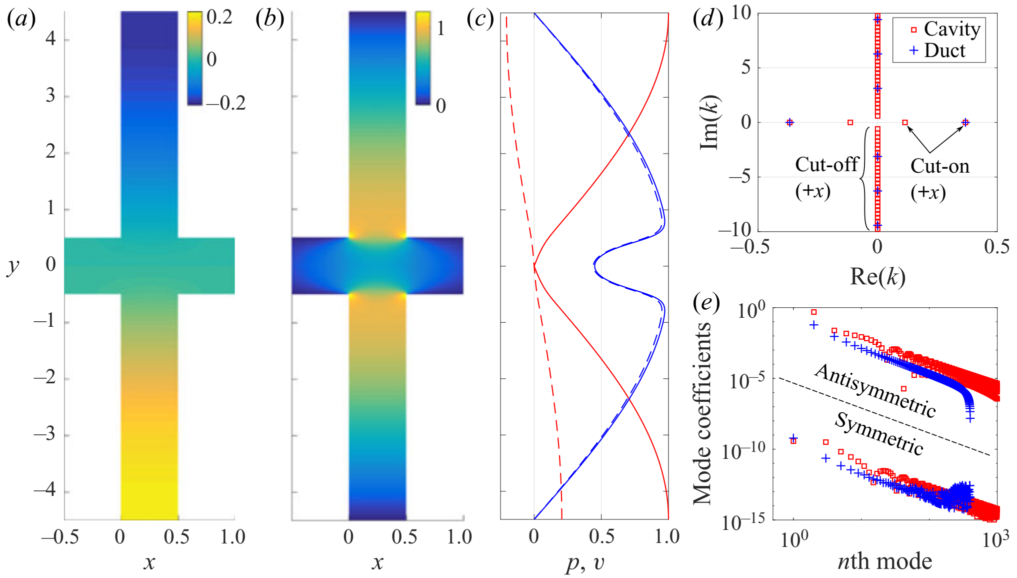

Figure 7. Spatial distribution of (*a*) Re(p) and (*b*) Re(v) of the antisymmetric acoustic resonant mode at a real-valued frequency $\omega_A = 0.3673$ (a trapped mode). (*c*) Variation of p (red) and v (blue) along y at $x = L/2$. Dashed lines, Re(p) and Re(v); solid lines, $|p|$ and $|v|$. (*d*) Wavenumbers of the travelling waves. (*e*) Mode coefficients of the travelling waves in the $+x$ direction, where the modes are sorted according to their orders. The legend in (*d*) also applies to (*e*).

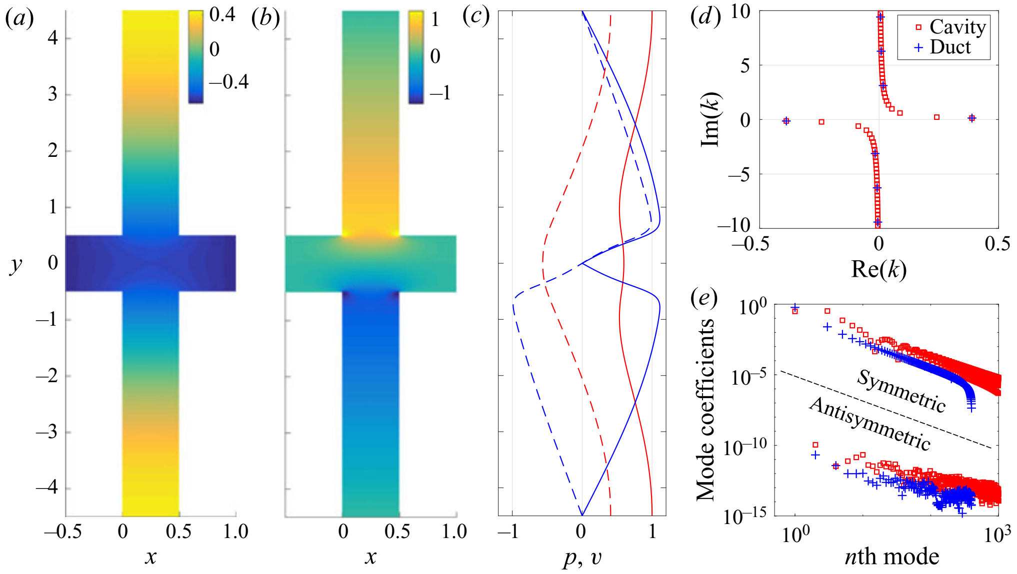

Figure 8. Spatial distribution of (*a*) Re(p) and (*b*) Re(v) of the symmetric acoustic resonant mode at a complex frequency $\omega_A = 0.3885 + 0.1350\text{i}$. For the descriptions of (*c–e*), see figure 7.

and antisymmetric travelling modes in such a symmetric system can be seen: compared with the antisymmetric counterparts, the symmetric travelling modes have vanishingly small amplitudes. The zero amplitude of the outgoing propagative (cut-on) mode in each duct, as indicated numerically in figure 7(*e*) by the vanishingly small mode coefficient of the $n = 1$ mode in the duct, means that acoustic energy of the trapped mode cannot escape, and consequently the trapped mode occurs at a real-valued frequency. Such a wave trapping mechanism in a symmetric system, i.e. because of symmetric mismatch, the antisymmetric trapped mode is decoupled from the outgoing plane waves in the two semi-infinite ducts which are the only cut-on modes in the ducts at the trapped mode frequency, has been extensively studied (Evans & Linton 1991; Evans, Levitin & Vassiliev 1994; Evans & Porter 1997; Pagneux 2013). The symmetric acoustic resonant mode, shown in figure 8(*a–c*), is assembled by symmetric travelling modes. The non-vanishing amplitude of the outgoing propagative mode in each duct, as shown in figure 8(*e*), means radiation of acoustic energy to infinity, thus the resonant mode is damped. Owing to the outgoing propagative modes in the ducts, $|k_{fl}| < 1$ if the frequency remains real valued. To satisfy the feedback-loop closure principle for a resonant mode ($k_{fl} = 1$), $\mathrm{Im}(\omega)$ increases. As shown in figure 8(*d*), for the two $+x$ propagative modes in the cavity segment $\mathrm{Im}(k) > 0$, since $\mathrm{Im}(\omega_A) > 0$.

The acoustic resonance frequency of the configuration can be approximately estimated with a one-dimensional model, assuming a resonance happens when $\lambda/2 = H + 2D$ or $\lambda/4 = D$, where λ is the wavelength. However, the two resonant modes shown in figures 7 and 8 are close to but not exactly the same as the $\lambda/2$-resonance between the two cavity bottoms (see figure 7*c*) or the $\lambda/4$-resonance in each cavity (see figures 7*c* and 8*c*). The $\lambda/2$- and $\lambda/4$-resonance frequencies are $\omega_{\lambda/2} = 0.3491$ and $\omega_{\lambda/4} = 0.3927$. In the present case, $\omega_{\lambda/2} < \omega_{A,anti} < \mathrm{Re}(\omega_{A,sym}) < \omega_{\lambda/4}$. The discrepancies in frequency depend on the geometrical parameters, and in general they reduce as the cavity depth is increased (Koch 2005; Hein *et al.* 2012). It is noted here that for $D/L = 1$ in § 3.1, the lowest acoustic resonance frequency is $\omega_{A,anti} = 1.9387$ when $R = 0$, which is much higher than the frequency range considered there.

For a comparison later in § 3.3, the acoustic resonant modes for the configuration $D/L = 8$ without flow but with a resistive sheet $R = 0.018$ added at the entrance of each cavity are also calculated here. The complex frequencies of the first antisymmetric and symmetric resonant modes are respectively $\omega_A = 0.3761 + 0.0044\mathrm{i}$ and $\omega_A = 0.3881 + 0.1415\mathrm{i}$, which indicate that the influence of the small R on $\mathrm{Re}(\omega_A)$ is extremely small and $\mathrm{Im}(\omega_A)$ is only slightly increased owing to the damping effect of R. Note that since the symmetry holds after the resistive sheets are introduced, the antisymmetric resonant mode, a lightly damped mode, however, is still a trapped mode (the outgoing propagative mode in each duct still has a zero amplitude).

The resonant modes presented in figures 7 and 8 are eigensolutions without forcing. As an acoustic forcing is introduced from the left duct, the wave scattering of the resonator is shown in figure 9, which is used to further discuss the purely acoustic resonances in figures 7 and 8 where $R = 0$, and to provide the forced acoustic fields inside the deep cavities at and far from the acoustic resonance frequencies that will be compared with the global modes in § 3.3 where $R \neq 0$. The calculation of wave scattering based on the scattering matrix method has been described in Dai & Aurégan (2018) and Dai (2020). The plane-wave transmission and reflection coefficients of the resonator are plotted in figure 9(*a*), which shows a zero transmission caused by the symmetric resonant mode. As the difference between the incident frequency and the resonant mode frequency is increased, the amplitude of the excited oscillations in the resonator decreases, as shown in figure 9(*d–f*). The antisymmetric resonant mode cannot be excited by an incoming

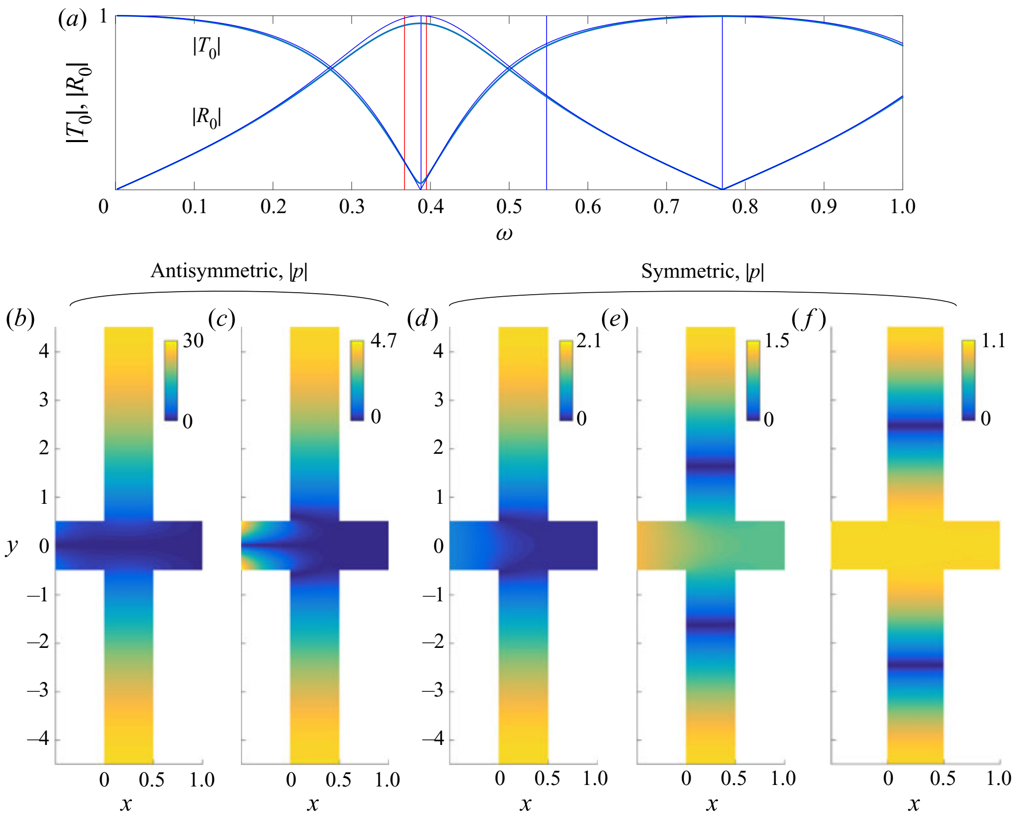

Figure 9. (*a*) Transmission and reflection coefficients for a plane-wave excitation (thin lines: $R = 0$, thick lines: $R = 0.018$). (*b*,*c*) Value of $|p|$ excited by the first $+x$ cross-mode in the left duct of amplitude $|p|_{max} = 1$ at $x = 0$, at frequencies denoted by red vertical lines in (*a*): $\omega = \mathrm{Re}(\omega_A)$ where $\omega_A = 0.3761 + 0.0044\mathrm{i}$ (antisymmetric acoustic resonance) and $\omega = 0.3949$ (frequency in figure 12*e*). (*d*–*f*) Value of $|p|$ excited by the $+x$ plane wave in the left duct of amplitude $|p| = 1$, at frequencies denoted by blue vertical lines in (*a*): $\omega = \mathrm{Re}(\omega_A)$ where $\omega_A = 0.3881 + 0.1415\mathrm{i}$ (symmetric acoustic resonance), $\omega = 0.5476$ (frequency in figure 14*d*) and $\omega = 0.7708$ (acoustic anti-resonance). In (*b*–*f*), $R = 0.018$.

plane wave owing to symmetric mismatch, thus its effect is not seen in figure 9(*a*). In figure 9(*b*,*c*), the resonator is excited by the first $+x$ cross-mode in the left duct. At the frequency of the antisymmetric resonant mode, the forcing excites a stronger oscillation in the resonator compared with figure 9(*d*–*f*), since the antisymmetric resonance has a larger quality factor. Note that, when $R = 0$, the quality factor of such a perfect resonance is infinity and the amplitude of response is also infinity. The present numerics indicate the pressure amplitude at the cavity bottoms shown in figure 9(*b*) to be $|p| = 1.15 \times 10^8$ if $R = 0$. In figure 9 and § 3.3, the pressure is shown in $|p|$ rather than $\mathrm{Re}(p)$ for a better visual comparison (see the acoustic pressure nodes inside the deep cavities in figures 9(*e*,*f*) and 14(*d*,*e*)). At $y = 0$, $|p| = 0$ and $|p| \neq 0$ respectively indicate antisymmetric and symmetric resonant modes.

3.3. *Vortical–acoustic resonance in an AR*

The problem sketched in figure 1(*b*) is discussed in this subsection. At low Mach numbers, the KH + RPR feedback loop occurring at the junction between the flow duct and the deep

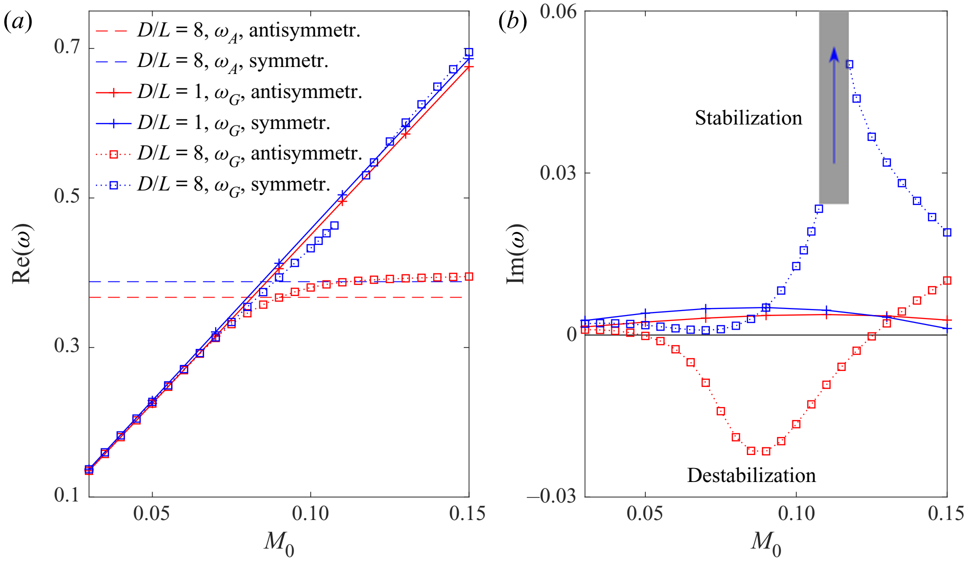

Figure 10. Global mode frequency ω_G as a function of M_0: comparison between the deep-cavity case ($D/L = 8$) and the shallow-cavity case ($D/L = 1$). In (*a*), ω_A of acoustic resonant modes ($0.3671 + 0.0044\mathrm{i}$ and $0.3881 + 0.1415\mathrm{i}$) are calculated with $R = 0.018$ without flow. The legend in (*a*) also applies to (*b*).

cavities is still acoustically compact, but this compact region is influenced by the acoustics of the resonator (Peters 1993; Kriesels *et al.* 1995).

The global mode frequency as a function of the Mach number is plotted in figure 10. At $M_0 = 0.03$, the global mode frequency for $D/L = 8$, being very close to those for $D/L = 1$, approximately agrees with the Strouhal law. As M_0 increases, $\mathrm{Re}(\omega_G)$ of the antisymmetric mode progressively deviates from the Strouhal law, and the deviation becomes more noticeable as $\mathrm{Re}(\omega_G)$ gets close to the frequency of the antisymmetric acoustic resonant mode, $\mathrm{Re}(\omega_A)$. The temporal growth rate, $-\mathrm{Im}(\omega_G)$, shows a global mode destabilization when $\mathrm{Re}(\omega_G)$ is around $\mathrm{Re}(\omega_A)$, and a maximum temporal growth rate occurs when $\mathrm{Re}(\omega_G) = \mathrm{Re}(\omega_A)$ (Yamouni *et al.* 2013), which in this case happens at $M_0 \approx 0.09$. Note that the acoustic resonance frequency might be slightly shifted owing to the convection of the acoustic waves by the flow. This shift, however, should be extremely small since the flow speed is low, thus the maximum temporal growth rate happens when $\mathrm{Re}(\omega_G)$ equals to the $\mathrm{Re}(\omega_A)$ calculated without flow. For the symmetric modes, the influence of the heavily damped acoustic resonant mode on the global modes is rather weak near the frequency crossing point. The deviation of $\mathrm{Re}(\omega_G)$ from the Strouhal law is small. However, $\mathrm{Im}(\omega_G)$ shows a stabilization phenomenon over a M_0 range where $\mathrm{Re}(\omega_G)$ is much larger than $\mathrm{Re}(\omega_A)$. It is noted that, in the grey region in figure 10(*b*) (also in figure 15), $\mathrm{Im}(\omega_G)$ is high. For example, $\omega_G = 0.5213 + 0.0843\mathrm{i}$ when $M_0 = 0.11$. We do not try to find the M_0 at which a peak $\mathrm{Im}(\omega_G)$ occurs, but mark that region in grey.

The different $\mathrm{Im}(\omega_G)$ trajectories of the antisymmetric and symmetric global modes explain the previous experiments, from a linear point of view, that vortex structures are not shed simultaneously from the upper and lower cavity leading edges but with a shift of half a period (Peters 1993; Kriesels *et al.* 1995; Oshkai & Yan 2008; Wang, Deng & Liu 2018). Note that both antisymmetric and symmetric global modes could be unstable near the crossing point of $\mathrm{Re}(\omega_G)$ and $\mathrm{Re}(\omega_A)$ if the shear layer thickness is reduced, but the antisymmetric one should win in the competition owing to its larger temporal growth rate.

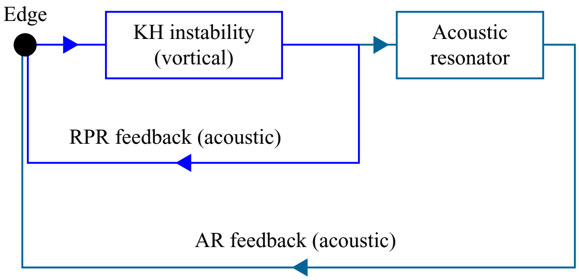

Figure 11. Vortical–acoustic resonance in an AR: KH instability and dual feedbacks. Adapted from Rienstra & Hirschberg (2018).

To explain the different ω_G trajectories of the antisymmetric and symmetric global modes in figure 10, we adopt the view sketched in figure 11 that the vortical–acoustic resonance in an acoustic resonator and the associated system instability are governed by the KH instability waves and dual feedbacks: the RPR and AR feedbacks (Powell 1990; Fabre & Hirschberg 2000; Rienstra & Hirschberg 2018).

The spatial distributions of the antisymmetric (figures 12 and 13) and symmetric (figure 14) global modes are plotted for different M_0, where the fields have been normalized by v at $x = L/4$ and $y = -H/2$. Figures 12(a,f) and 14(a,f) show that, when $\mathrm{Re}(\omega_G)$ is much lower than $\mathrm{Re}(\omega_A)$, at a very low Mach number $M_0 = 0.03$, the acoustic effect of the resonator barely shows in the spatial distributions, i.e. the whole resonator is compact. As $\mathrm{Re}(\omega_G)$ increases with the increasing M_0, the acoustic effect of the resonator on the $|p|$ distribution progressively appears. Note in figure 10(a) that, for global and acoustic resonant modes of the same symmetry, $\mathrm{Re}(\omega_G)$ only coincides with $\mathrm{Re}(\omega_A)$ at one particular value of M_0 as $\mathrm{Re}(\omega_G)$ varies continuously with M_0, since the antisymmetric or symmetric acoustic resonant mode only occurs at one discrete frequency in the frequency range considered. However, the influence of the resonator on the global modes appears over continuous Mach number and frequency ranges. It is also interesting to compare the $|p|$ distribution here with those shown in figure 9. The excitation frequencies in figures 9(c) and 9(e) respectively equal to $\mathrm{Re}(\omega_G)$ in figures 12(e) and 14(d). The resemblance in the $|p|$ distribution inside the cavities can be observed when the frequencies coincide, even though one is an externally excited field whereas the other is an eigenfunction describing the two-way excitation between vortical and acoustic motions in an AR.

Note that the different variation in $|p|$ at the cavity bottoms with frequency shown in figures 12–14 from those in figure 9 might be due to the compressibility effect changing with M_0 and also the variation in global mode distribution (the global modes are normalized by v at a constant position).

We now analyse the phase relation and the Strouhal number. The variations of v along the line between the upstream and downstream edges of the lower cavity are plotted in the third and fourth columns in figures 12–14. By observing those variations, one can analyse the effect of the AR on the KH + RPR loop that mainly happens at the cavity openings. For the antisymmetric modes, figure 12(p,q,r,s,t) shows that the phase difference of the vortical disturbances between the edges reduces as M_0 is increased. Nevertheless, the phase difference of the $-x$ acoustic disturbances between the edges also changes with M_0, and the total phase variation around the feedback loop, which is approximately represented by the phase variation of the vortical disturbances from the upstream to the downstream edge plus the phase variation of the $-x$ acoustic disturbances from the downstream to the upstream edge, remains close to an integral multiple of 2π. For the symmetric

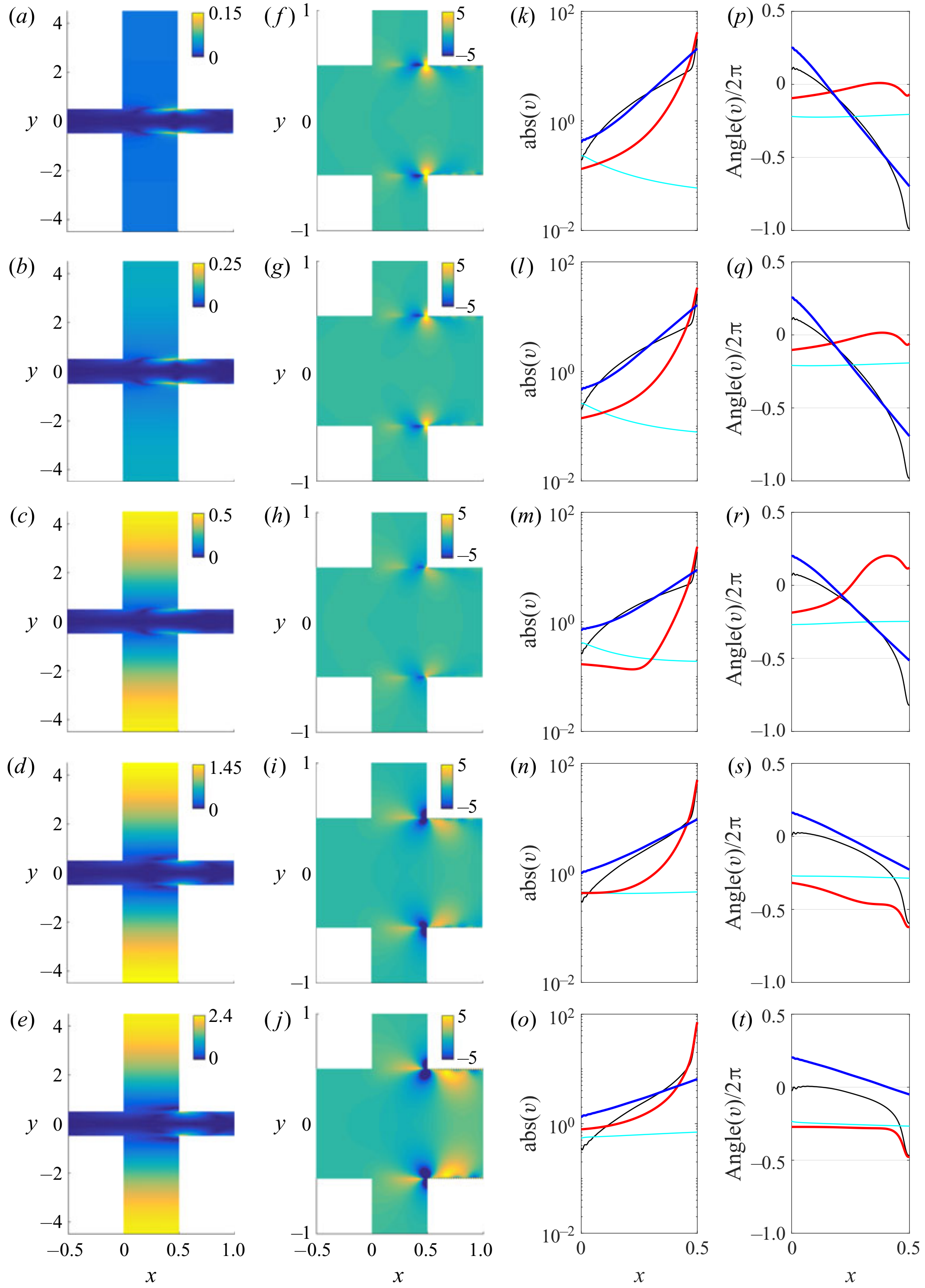

Figure 12. Spatial distributions of the antisymmetric global modes for $M_0 = 0.03$, 0.06, 0.09, 0.12 and 0.15 (rows 1 to 5). Column 1, $|p|$; column 2, $\mathrm{Re}(v)$; columns 3 and 4, amplitude and phase of v along the opening of the low cavity (at the point just below $y = -H/2$). Blue lines, vortical; red lines, $-x$ acoustic; cyan lines, $+x$ acoustic; black lines, total (all travelling modes).

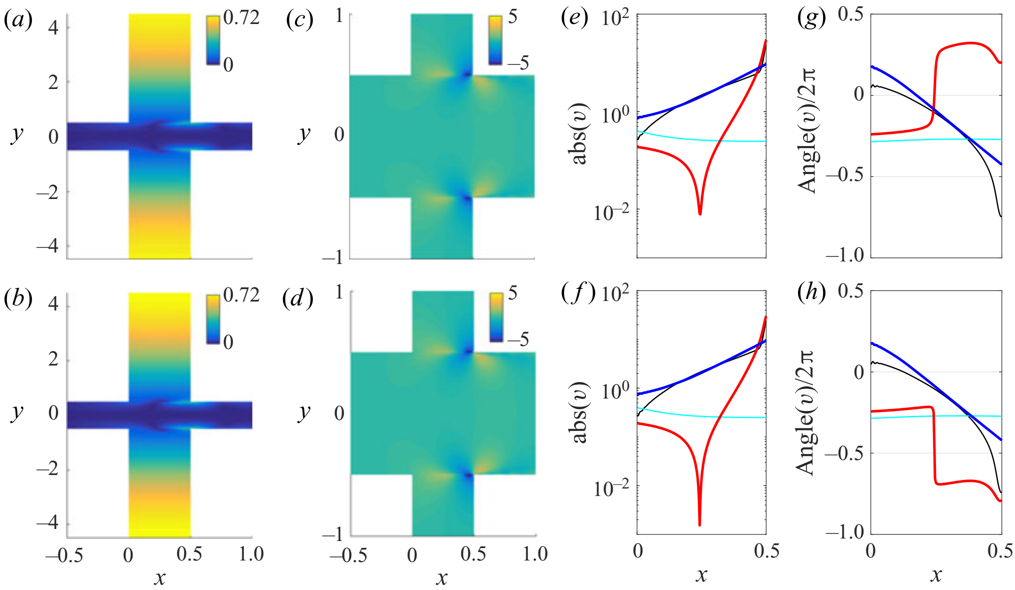

Figure 13. Spatial distributions of the antisymmetric global modes for $M_0 = 0.0985$ (row 1, $\omega_G = 0.3787 - 0.0175\mathrm{i}$) and 0.0990 (row 2, $\omega_G = 0.3792 - 0.0172\mathrm{i}$), between which the mode switching occurs. See figure 12 for the descriptions of the columns.

modes, figure 14(*p,q,r,s,t*) shows that the variation of the phase difference of the vortical disturbances between the edges with the increasing M_0 is small. The phase variations are further displayed in figure 15(*a,b*), which shows that the variation of the phase difference of the KH waves between cavity edges is directly linked to the $-x$ acoustic disturbances, required by loop closure.

An interpretation of the variation of the KH phase difference between the upstream and downstream edges in the antisymmetric and symmetric global modes, from the dual-feedback view, is as follows. In the antisymmetric global modes in figure 12, the acoustic resonant mode is a nearly perfect resonant mode with a high quality factor, as discussed in § 3.2. At frequencies near $\mathrm{Re}(\omega_A)$, the AR feedback, having an amplitude much higher than that of the RPR feedback at the cavity leading edges, dominates in the total feedback. Thus, the quick variation of the KH phase difference near $\mathrm{Re}(\omega_A)$ is due to the quick phase change with frequency in the response function of the AR (Tonon *et al.* 2011). On the other hand, the heavily damped symmetric acoustic resonant mode has a minor influence on the loop phase relation in figure 14, since the corresponding response function has a low magnitude and a slowly varying phase.

The Strouhal number defined as $Sr = \mathrm{Re}(\omega_G)L/2\pi M_0$ is reformed,

$$Sr = \frac{\mathrm{Re}(\omega_G)L}{2\pi M_c}\frac{M_c}{M_0}, \tag{3.1}$$

where M_c is the convection velocity of the KH waves. The first term on the right-hand side of (3.1) equals the ratio between the cavity length and the KH wavelength, and equals the phase difference of the KH waves between cavity edges, i.e. $\Delta\phi_{KH}/2\pi = L/\lambda_{KH} = \mathrm{Re}(\omega_G)L/2\pi M_c$. Thus, the essential mechanism of the frequency deviation from the Strouhal law shown in figure 10(*a*), which reflects the deviation of $\Delta\phi_{KH}$ from 2π, is the upstream feedback being affected by the AR, or the coexistence of RPR and

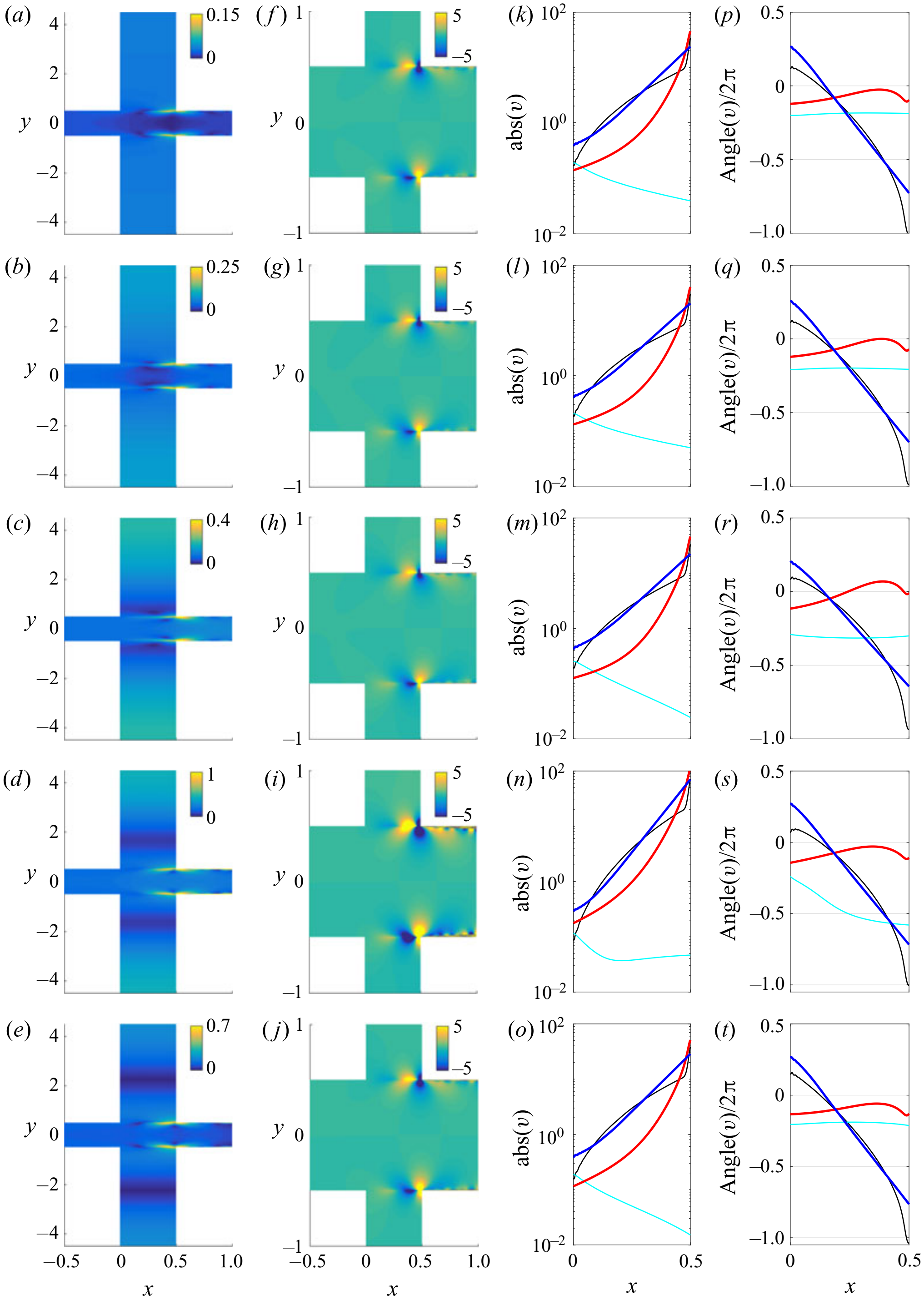

Figure 14. Spatial distributions of the symmetric global modes for $M_0 = 0.03$, 0.06, 0.09, 0.12 and 0.15 (rows 1 to 5). See figure 12 for the descriptions of the columns.

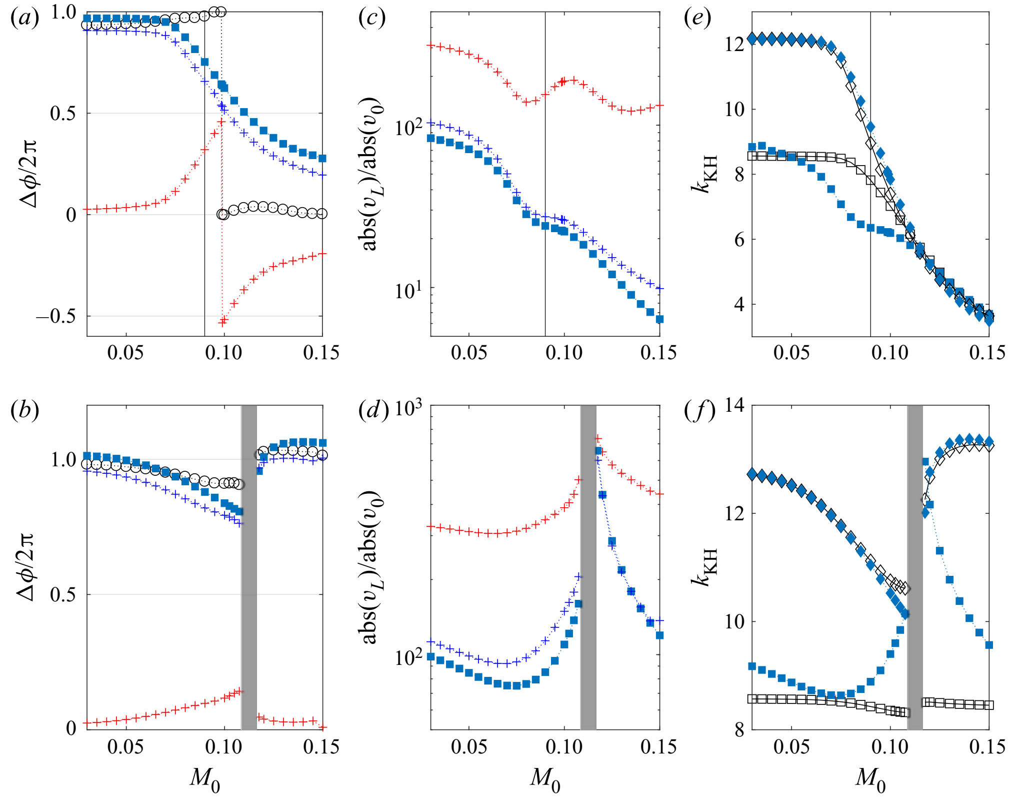

Figure 15. Phase difference (a,b) and amplitude ratio (c,d) of v at the upstream and downstream cavity edges (blue and red crosses, $\pm x$ disturbances; solid squares, the KH waves; circles, the phase change of $-x$ disturbances plus the phase change of $+x$ disturbances). (e,f) Wavenumbers of the KH waves (solid squares and diamonds, Re(k_{KH}) and Im(k_{KH}) calculated with ω_G; hollow squares and diamonds, Re(k_{KH}) and Im(k_{KH}) calculated with Re(ω_G)). Rows 1 and 2: antisymmetric and symmetric global modes.

AR feedbacks. Note that for a parallel velocity profile, M_c/M_0 also depends on Sr (Michalke 1965; Schmid & Henningson 2001), and this relation also influences the finally selected frequency of a global mode.

It is shown in figure 10(a) that the reduction of the Strouhal number of the antisymmetric global modes continues even though M_0 is no longer close to $M_0 = 0.09$. This might be linked to the global mode switching, that is, the total phase change around the feedback loop jumping from $2j\pi$ to $2(j-1)\pi$, where j is an integer. The mode switching is shown in figures 12(r,s) and 15(a). Here, the switching happens slightly later than the maximum temporal growth rate as M_0 is increased, which is in line with the result of Yamouni *et al.* (2013). The switching is found to occur suddenly during the increase of M_0. Figure 13 elaborates the mode switching and shows that the switching is linked to the $-x$ acoustic disturbances. The $\pm\pi$ phase jump and the zero amplitude suggest that v of the $-x$ acoustic disturbances changes sign between the downstream and upstream edges. Such a phenomenon, not happening in the compact case, indicates the interaction between the RPR and AR feedbacks here. Note that the phase jump can only be observed near the entrance of the cavities ($y = \pm H/2$) where both the KH + RPR loop and the additional AR feedback are at play. At positions inside the deep cavities, the disturbance field, almost completely governed by the AR, is uniform in the x direction. The phase jump happening in the $-x$ acoustic disturbances rather than in the KH wave also suggests that the mode switching is not a vortical but an acoustic effect.

The present linear global mode analysis for the compact and deep-cavity cases might also provide some insight into the frequency lock-in phenomenon in experiments. In the compact case, since the phase difference of the KH waves between the edges is almost constant and approximately equals to 2π, owing to the fact that the solo RPR feedback is nearly hydrodynamic, the oscillation frequency roughly follows the Strouhal law. When an AR is involved, the total feedback is affected by the additional AR feedback, thus $\Delta\phi_{KH}/2\pi$ accordingly changes to satisfy the loop phase relation. Moreover, $\Delta\phi_{KH}/2\pi$ varies quickly with frequency when $\mathrm{Re}(\omega_G)$ is near the $\mathrm{Re}(\omega_A)$ of an acoustic resonant mode which has a small $\mathrm{Im}(\omega_A)$. Such a linear mechanism of frequency deviation from the Strouhal law is described in this work. It is noted that a linear mode-coupling mechanism has also been discussed for the frequency lock-in in vortex-induced vibrations (de Langre 2006). The measured frequency of self-sustained cavity flow oscillations also depends on the oscillation amplitude which affects the convection velocity of the vortical motions (M_c/M_0). At high amplitudes, the shear layer, strongly perturbed by the intense feedback acoustic waves at the separation point, rolls up into concentrated vortex structures (Ho & Huerre 1984). A minimum value of M_c/M_0 happens at the Mach number of maximum oscillation amplitude (Ma *et al.* 2009). In some cases, clear vortex structures may not be observed, but the shear layer can be thickened by medium amplitude oscillations, which also leads to a decrease of the convection velocity (Boujo, Bauerheim & Noiray 2018).

The coexistence of the RPR and AR feedbacks also explains the stabilization and destabilization shown in figure 10(*b*). As shown in the compact case in § 3.1, the amplitude of the RPR feedback disturbances is very small at the upstream separation points. For the antisymmetric modes in the deep-cavity case, the AR feedback is strong near the frequency of the acoustic resonant mode. Thus, compared with the solo RPR feedback, the amplitude of $-x$ acoustic disturbances at the leading edges is increased in the deep-cavity case, which decreases the ratio between the amplitudes of the $-x$ feedback disturbances at $x = L$ and at $x = 0$. For the symmetric modes, the weak AR feedback at the upstream edge may have a comparable amplitude as the RPR feedback but an opposite phase. Those two feedbacks then cancel each other at the upstream edge, which leads to an extremely large ratio between the amplitudes of the $-x$ feedback disturbances at $x = L$ and at $x = 0$. To satisfy the amplitude relation of the feedback loop for a global mode, the imaginary part of the frequency should be adjusted (see discussion in figure 6). The above analysis is clearly confirmed in figure 15(*d*) for the symmetric global modes, even though the plot only approximately represents $\boldsymbol{P}_u$ and $\boldsymbol{P}_d$ of the feedback loop. It demonstrates the large ratio between $|v|$ at the downstream edge and $|v|$ at the upstream edge, for the $-x$ feedback disturbances owing to the mutual cancellation between RPR and AR feedbacks at the upstream edge and also for the symmetric KH mode owing to the amplitude requirement for loop closure. The large $\mathrm{Im}(k_{\mathrm{KH}})$ indicated in figure 15(*d*) is linked to the increase of $\mathrm{Im}(\omega_G)$ (stabilization), as shown in figure 15(*f*). For the antisymmetric global modes, $|v|$ ratios for the $-x$ feedback disturbances and for the KH wave do not show the same trend, as shown in figure 15(*c*), which seems due to the global mode switching. A simple and intuitive demonstration of the feedback-loop destabilization is not obtained at this moment, although figure 15(*e*) shows the reduction of $\mathrm{Im}(k_{\mathrm{KH}})$ over the M_0 range of destabilization.

4. Conclusion

Vortical–acoustic resonance in 2-D symmetric duct–cavity configurations is studied by a linear global mode analysis about a low-speed inviscid parallel shear flow. In practice, even in the linear regime, the shear layer over a cavity develops, thus both convection velocity and spatial growth rate of vortical disturbances vary across the cavity. Because of the longitudinal-homogeneity and inviscid-flow assumptions and the added resistance in the calculations, the present results are of qualitative interest only. Nevertheless, such a mean flow model renders a neat separation of vortical and acoustic disturbances and a combined travelling–global mode analysis, which offer insight into some essential mechanisms involved.

First, in a shallow-cavity case, results are in line with the previous understanding of the Rossiter modes in compact cases. Vortical–acoustic resonance and the associated global instability, owing to the KH instability and the RPR feedback, can be supported by an incompressible model, where the feedback disturbances are purely hydrodynamic. The difference between incompressible and compressible models in describing the compact KH + RPR feedback loop at low flow speeds is small. The phase difference of the unstable vortical waves between the upstream and downstream cavity edges is close to 2π, i.e. $\Delta\phi_{KH}/2\pi \approx 1$, and the global mode frequency agrees with the Strouhal law.

The influence of an AR on the KH + RPR feedback loop is then examined. Note that, for symmetric configurations, the split between antisymmetric and symmetric travelling modes occurs in both acoustic and vortical–acoustic resonant modes. In this deep-cavity case, two acoustic resonant modes occur in the frequency range considered: the antisymmetric one is a trapped mode (lightly damped by the resistive sheets introduced in the calculations) whereas the symmetric one is a heavily damped mode due to radiation. As the Mach number is increased, different trajectories of the antisymmetric and symmetric global modes are observed. The frequency of the antisymmetric global modes deviates from the Strouhal law and the global modes are destabilized when the global mode frequency is close to the frequency of the antisymmetric acoustic resonant mode. A global mode switching is also observed. On the other hand, the influence of the symmetric acoustic resonant mode on the global modes is much smaller. Nevertheless, a stabilization of the symmetric global modes is observed. We have shown that the global mode-related phenomena can be explained by the local–global relation of the feedback loop and the dual-feedback view: the coexistence of the RPR and AR feedbacks. The frequency deviation from the Strouhal law is due to $\Delta\phi_{KH}/2\pi$ being changed by the additional AR feedback, and $\Delta\phi_{KH}/2\pi$ changes quickly with frequency when the global mode frequency is near the frequency of an acoustic resonant mode with a high quality factor, such as a trapped mode. Such a linear result provides some insight into the frequency lock-in phenomenon in experiments, although the frequency of self-sustained cavity flow oscillations also depends on the oscillation amplitude. It is found that the global mode switching is not a vortical but an acoustic effect. The switching results from the interaction between the RPR and AR feedbacks, whereas the vortical motions do not show signs of the sudden switching. The global mode destabilization and stabilization are respectively understood as the result of the total feedback at the upstream edge being strengthened and weakened by the additional AR feedback.

Funding. This work has been supported by the National Natural Science Foundation of China no. 51876120.

Declaration of interests. The author reports no conflict of interest.

Author ORCIDs.
Xiwen Dai https://orcid.org/0000-0002-9370-9048.

Case	N_1	ω_G
GM1	400	$3.6678 \times 10^{-1} - 2.1521 \times 10^{-2}\mathrm{i}$
GM1	600	$3.6658 \times 10^{-1} - 2.1651 \times 10^{-2}\mathrm{i}$
GM1	800	$3.6651 \times 10^{-1} - 2.1693 \times 10^{-2}\mathrm{i}$
GM1	1000	$3.6647 \times 10^{-1} - 2.1710 \times 10^{-2}\mathrm{i}$
GM2	400	$5.4759 \times 10^{-1} + 4.3785 \times 10^{-2}\mathrm{i}$
GM2	600	$5.4616 \times 10^{-1} + 4.3132 \times 10^{-2}\mathrm{i}$
GM2	800	$5.4567 \times 10^{-1} + 4.2907 \times 10^{-2}\mathrm{i}$
GM2	1000	$5.4544 \times 10^{-1} + 4.2802 \times 10^{-2}\mathrm{i}$

Table 1. Convergence assessment of the numerical calculations.

Appendix A. Convergence of calculations

The convergence of the present numerical calculations is assessed on table 1, using two global modes for $D/L = 8$ for example: GM1, the antisymmetric mode at $M_0 = 0.09$; GM2, the symmetric mode at $M_0 = 0.12$.

Appendix B. Multiple feedback-loop channels

Since in each system resonant mode there are multiple downstream- and upstream-travelling modes in the cavity segment, the feedback loop can be seen as the sum of multiple channels, each of which is associated with one downstream-travelling mode, one upstream-travelling mode and their mutual reflection at the segment ends. A preliminary analysis of the multiple feedback-loop channels is performed in figure 16 for the antisymmetric global modes of the compact and deep-cavity configurations. The wavenumbers in figure 16(*a*,*b*) show that the decay rates of several $-x$ acoustic modes are less than or comparable to the growth rates of the KH modes, thus all those $-x$ acoustic modes are possible candidates for closing the loop, from the loop-gain consideration.

In the antisymmetric Rossiter mode of the compact case, the $\pm x$ acoustic plane waves are not involved in the feedback loop owing to symmetric mismatch, as indicated by their vanishingly small coefficients in figure 16(*c*), thus the $-x$ acoustic modes closing the loop are all evanescent modes, among which the least attenuated mode has the highest amplitude at the upstream end. To examine the error of using a KH mode plus some less attenuated $-x$ acoustic modes to represent the Rossiter mode, the channel gain is calculated. Assuming that the mth element in $\boldsymbol{C}_{fl}$ is the coefficient of the antisymmetric KH mode, the loop gain of the channel consisting of the KH mode and the nth $-x$ acoustic mode is $G_{KH,n} = |\boldsymbol{M}_u(m,n) \times \boldsymbol{M}_d(n,m)|$, where $\boldsymbol{M}_u = \boldsymbol{R}_u\boldsymbol{P}_u$, $\boldsymbol{M}_d = \boldsymbol{R}_d\boldsymbol{P}_d$, m and n denotes the positions of the elements in the matrices. The result of $G_{KH,n}$ is plotted in 16(*e*), which shows that the first antisymmetric channel has the largest gain 0.817. The sum of the gains of N_2 channels is $G_{KH} = |\sum_n \boldsymbol{M}_u(m,n) \times \boldsymbol{M}_d(n,m)| = |\boldsymbol{M}_{fl}(m,m)| = 0.915$, which is close to but less than unity, denoting an amplitude variation of the KH mode after the loop through the N_2 acoustic channels. This indicates the effect of the other $+x$ travelling modes on the replication of the KH mode around a feedback loop. For the global mode in the deep-cavity case, $G_{KH} = 0.292$. The global mode is now governed by the KH + RPR loop, which may still be approximately described by a KH mode plus some less attenuated $-x$ acoustic modes, and the additional AR effect. In the travelling-mode representation of the latter, some $+x$ acoustic modes are as significant as their $-x$ counterparts, as indicated by the pressure distributions inside the deep cavities

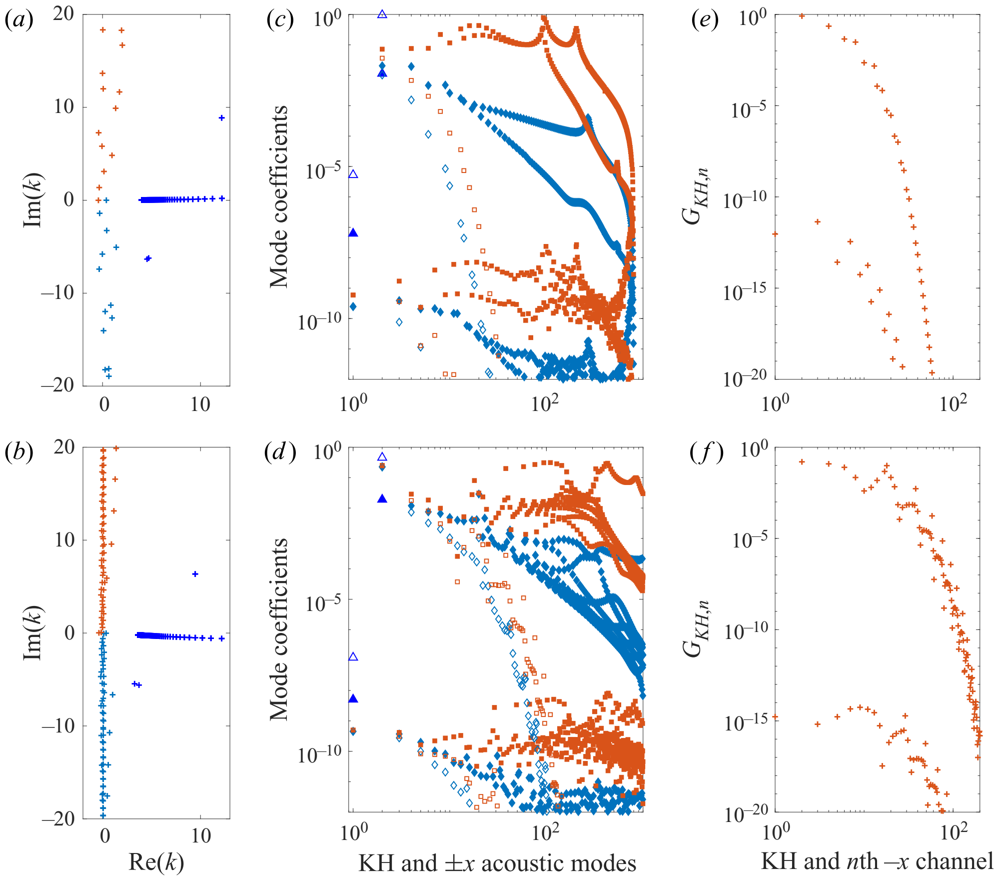

Figure 16. Multiple feedback-loop channel analysis of two antisymmetric global modes (row 1, figure 2(*a*,*c*), $D/L = 1$ and $M_0 = 0.9$; row 2, figure 12(*c*,*h*), $D/L = 8$ and $M_0 = 0.9$). (*a*,*b*) Wavenumbers in the cavity segment, (*c*,*d*) mode coefficients of the KH and ±*x* acoustic modes in the cavity segment (triangles, KH; diamonds, $+x$ acoustic; squares, $-x$ acoustic. Solid and hollow symbols respectively denote the coefficients at the segment ends where the wave travelling starts and terminates), (*e*,*f*) Loop gain of each channel consisting of the antisymmetric KH mode and a $-x$ acoustic mode.

in §§ 3.2 and 3.3. Nevertheless, at the cavity openings ($y = \pm H/2$), $|v|$ associated with the group of the $+x$ acoustic modes is negligibly small compared with those of the vortical and the $-x$ acoustic groups (see column 3 in figures 12–14), which simplifies the downstream–upstream analysis of the feedback loop done in § 3.3.

REFERENCES

ALVAREZ, J.O. & KERSCHEN, E.J. 2005 Influence of wind tunnel walls on cavity acoustic resonances. *AIAA Paper* 2005-2804.

ALVAREZ, J.O., KERSCHEN, E.J. & TUMIN, A. 2004 A theoretical model for cavity acoustic resonances in subsonic flow. *AIAA Paper* 2004-2845.

BARBAGALLO, A., SIPP, D. & SCHMID, P. 2009 Closed-loop control of an open cavity flow using reduced order models. *J. Fluid Mech.* **641**, 1–50.

BAUERHEIM, M., BOUJO, E. & NOIRAY, N. 2020 Numerical analysis of the linear and nonlinear vortex-sound interaction in a T-junction. *AIAA Paper* 2020-2569.

BLAKE, W.K. & POWELL, A. 1986 The development of contemporary views of flow-tone generation. In *Recent Advances in Aeroacoustics*, pp. 247–345, Springer.

Boujo, E., Bauerheim, M. & Noiray, N. 2018 Saturation of a turbulent mixing layer over a cavity: response to harmonic forcing around mean flows. *J. Fluid Mech.* **853**, 386–418.

Bruggeman, J.C., Hirschberg, A., van Dongen, M.E.H. & Wijnands, A.P.J. 1991 Self-sustained aero-acoustic pulsations in gas transport systems: experimental study of the influence of closed side branches. *J. Sound Vib.* **151**, 371–393.

Crighton, D. 1992 The jet edge-tone feedback cycle; linear theory for the operating stages. *J. Fluid Mech.* **234**, 361–391.

Dai, X. 2020 Flow–acoustic resonance in a cavity covered by a perforated plate. *J. Fluid Mech.* **884**, A4.

Dai, X. & Aurégan, Y. 2018 A cavity-by-cavity description of the aeroacoustic instability over a liner with a grazing flow. *J. Fluid Mech.* **825**, 126–145.

Dai, X., Jing, X. & Sun, X. 2015 Flow-excited acoustic resonance of a Helmholtz resonator: discrete vortex model compared to experiments. *Phys. Fluids* **27**, 057102.

Doaré, O. 2001 Instabilités locales et globales en interaction fluide–structure. PhD thesis, École Polytechnique.

Doaré, O. & de Langre, E. 2006 The role of boundary conditions in the instability of one-dimensional systems. *Eur. J. Mech.* (*B/Fluids)* **25**, 948–959.

East, L.F. 1966 Aerodynamically induced resonance in rectangular cavities. *J. Sound Vib.* **3**, 277–287.

Edgington-Mitchell, D. 2019 Aeroacoustic resonance and self-excitation in screeching and impinging supersonic jets–a review. *Intl J. Aeroacoust.* **18**, 118–188.

Evans, D.V., Levitin, M. & Vassiliev, D. 1994 Existence theorems for trapped modes. *J. Fluid Mech.* **261**, 21–31.

Evans, D.V. & Linton, C.M. 1991 Trapped modes in open channels. *J. Fluid Mech.* **225**, 153–175.

Evans, D.V. & Porter, R. 1997 Trapped modes about multiple cylinders in a channel. *J. Fluid Mech.* **339**, 331–356.

Fabre, B. & Hirschberg, A. 2000 Physical modeling of flue instruments: a review of lumped models. *Acustica* **86**, 599–610.

Ffowcs-Williams, J.E. 1969 Hydrodynamic noise. *Annu. Rev. Fluid Mech.* **1**, 197–222.

Fosas de Pando, M., Schmid, P.J. & Sipp, D. 2014 A global analysis of tonal noise in flows around aerofoils. *J. Fluid Mech.* **754**, 5–38.

Gallaire, F. & Chomaz, J.-M. 2004 The role of boundary conditions in a simple model of incipient vortex breakdown. *Phys. Fluids* **16**, 274.

Gharib, M. & Roshko, A. 1987 The effect of flow oscillations on cavity drag. *J. Fluid Mech.* **177**, 501–530.

Gloerfelt, X. 2009 *Cavity Noise*, von Kármán Lecture Notes on Aerodynamic Noise from Wall-bounded Flows. von Kármán Institute for Fluid Dynamics.

Gojon, R., Bogey, C. & Marsden, O. 2016 Investigation of tone generation in ideally expanded supersonic planar impinging jets using large-eddy simulation. *J. Fluid Mech.* **808**, 90–115.

Goldstein, M.E. 1978 Unsteady vortical and entropic distortions of potential flows round arbitrary obstacles. *J. Fluid Mech.* **89**, 443–468.

Hein, S., Hohage, T. & Koch, W. 2004 On resonances in open systems. *J. Fluid Mech.* **506**, 255–284.

Hein, S., Koch, W. & Nannen, L. 2012 Trapped modes and fano resonances in two-dimensional acoustical duct–cavity systems. *J. Fluid Mech.* **692**, 257–287.

Hellmich, B. & Seume, J.R. 2008 Causes of acoustic resonance in a high-speed axial compressor. *Trans. ASME J. Turbomach.* **130**, 031003.

Ho, C.M. & Huerre, P. 1984 Perturbed free shear layers. *Annu. Rev. Fluid Mech.* **16**, 365–424.

Howe, M.S. 1997 Edge, cavity and aperture tones at very low Mach numbers. *J. Fluid Mech.* **330**, 61–84.

Jensen, F.B., Kuperman, W.A., Porter, M.B. & Schmidt, H. 2011 *Computational Ocean Acoustics*, chap. 2 & 5. Springer.

Jordan, P., Jaunet, V., Towne, A., Cavalieri, A.V.G., Colonius, T., Schmidt, O. & Agarwal, A. 2018 Jet–flap interaction tones. *J. Fluid Mech.* **853**, 333–358.

Knisely, C. & Rockwell, D. 1982 Self-sustained low-frequency components in an impinging shear layer. *J. Fluid Mech.* **116**, 157–186.

Koch, W. 2005 Acoustic resonances in rectangular open cavities. *AIAA J.* **43**, 2342–2349.

Koch, W. 2009 Acoustic resonances and trapped modes in annular plate cascades. *J. Fluid Mech.* **628**, 155–180.

Kooijman, G., Hirschberg, A. & Aurégan, Y. 2010 Influence of mean flow profile and geometrical ratios on scattering of sound at a sudden area expansion in a duct. *J. Sound Vib.* **329**, 607–626.

Kooijman, G., Testud, P., Aurégan, Y. & Hirschberg, A. 2008 Multimodal method for scattering of sound at a sudden area expansion in a duct with subsonic flow. *J. Sound Vib.* **310**, 902–922.

KOOK, H. & MONGEAU, L. 2002 Analysis of the periodic pressure fluctuations induced by flow over a cavity. *J. Sound Vib.* **251**, 823–846.

KRIESELS, P.C., PETERS, M.C.A.M., HIRSCHBERG, A., WIJNANDS, A.P.J., IAFRATI, A., RICCARDI, G., PIVA, R. & BRUGGEMAN, J.C. 1995 High amplitude vortex-induced pulsations in a gas transport system. *J. Sound Vib.* **184**, 343–368.

LANDAU, L.D. & LIFSHITZ, E.M. 1981 *Physical Kinetics*, pp. 281–283. Pergamon.

DE LANGRE, E. 2006 Frequency lock-in is caused by coupled-mode flutter. *J. Fluids Struct.* **22**, 783–791.

DE LASSON, J.R., KRISTENSEN, P.T., MØRK, J. & GREGERSEN, N. 2014 Roundtrip matrix method for calculating the leaky resonant modes of open nanophotonic structures. *J. Opt. Soc. Am.* **31**, 2142–2152.

MA, R., SLABOCH, P.E. & MORRIS, S.C. 2009 Fluid mechanics of the flow-excited Helmholtz resonator. *J. Fluid Mech.* **623**, 1–26.

MARTINI, E., CAVALIERI, A.V.G. & JORDAN, P. 2019 Acoustic modes in jet and wake stability. *J. Fluid Mech.* **867**, 804–834.

MARX, D. & AURÉGAN, Y. 2013 Effect of turbulent eddy viscosity on the unstable surface mode above an acoustic liner. *J. Sound Vib.* **332**, 3803–3820.

MÉRY, F. 2010 Instabilités linéaires et rayonnement acoustique d'un écoulement sur une paroi présentant une cavité. PhD thesis, Université de Toulouse.

MICHALKE, A. 1965 On spatially growing disturbances in an inviscid shear layer. *J. Fluid Mech.* **23**, 521–544.

MILES, J.W. 1958 On the disturbed motion of a plane vortex sheet. *J. Fluid Mech.* **4** (5), 538–552.

NAKIBOGLU, G., BELFROID, S.P.C., GOLLIARD, J. & HIRSCHBERG, A. 2011 On the whistling corrugated pipes: effect of pipe length and flow profile. *J. Fluid Mech.* **672**, 78–108.

NAKIBOGLU, G., MANDERS, H.B.M. & HIRSCHBERG, A. 2012 Aeroacoustic power generated by a compact axisymmetric cavity: prediction of self-sustained oscillation and influence of the depth. *J. Fluid Mech.* **703**, 163–191.

NELSON, P.A., HALLIWELL, N.A. & DOAK, P.E. 1981 Fluid dynamics of a flow excited resonance. *J. Sound Vib.* **78**, 15–38.

OSHKAI, P. & YAN, T. 2008 Experimental investigation of coaxial side branch resonators. *J. Fluids Struct.* **24**, 589–603.

PAGNEUX, V. 2013 Trapped modes and edge resonances in acoustics and elasticity. In *Dynamic Localization Phenomena in Elasticity, Acoustics and Electromagnetism* (ed. R.V. Craster & J. Kaplunov), pp. 181–223, Springer.

PARKER, R. 1966 Resonance effects in wake shedding from parallel plates: some experimental observations. *J. Sound Vib.* **4**, 62–72.

PETERS, M.C.A.M. 1993 Aeroacoustic sources in internal flows. PhD thesis, Technische Universiteit Eindhoven.

POWELL, A. 1953 On edge tones and associated phenomena. *Acoustics* **3**, 233–243.

POWELL, A. 1961 On the edgetone. *J. Acoust. Soc. Am.* **33**, 395–409.

POWELL, A. 1990 Some aspects of aeroacoustios: from Rayleigh until today. *J. Vib. Acoust.* **112**, 145–159.

POWELL, A. 1995 Lord Rayleigh's foundations of aeroacoustics. *J. Acoust. Soc. Am.* **98**, 1839–1844.

RAYLEIGH, LORD 1945 *The Theory of Sound*, vol. 2. Dover.

RIENSTRA, S.W. & HIRSCHBERG, A. 2018 *An Introduction to Acoustics*. Eindhoven University of Technology.

ROCKWELL, D. & NAUDASCHER, E. 1978 Review self-sustaining oscillations of flow past cavities. *Trans. ASME J. Fluids Engng* **100**, 152.

ROSSITER, J.E. 1964 Wind-tunnel experiments on the flow over rectangular cavities at subsonic and transonic speeds. *Aero. Res. Counc. R&M*, No. 3438.

ROWLEY, C.W. & WILLIAMS, D.R. 2006 Dynamics and control of high-Reynolds-number flow over open cavities. *Annu. Rev. Fluid Mech.* **38**, 251–276.

ROWLEY, C.W., WILLIAMS, D.R., COLONIUS, T., MURRAY, R.M. & MACMYNOWSKI, D.G. 2006 Linear models for control of cavity flow oscillations. *J. Fluid Mech.* **547**, 317–330.

SCHMID, P.J. & HENNINGSON, D.S. 2001 *Stability and Transition in Shear Flows*. Springer.

SIPP, D., MARQUET, O., MELIGA, P. & BARBAGALLO, A. 2010 Dynamics and control of global instabilities in open-flows: a linearized approach. *Appl. Mech. Rev.* **63**, 030801.

STEWART, P.S., WATERS, S.L. & JENSEN, O.E. 2009 Local and global instabilities of flow in a flexible-walled channel. *Eur. J. Mech.* (B/*Fluids)* **28**, 541–557.

STONEMAN, S.A.T., HOURIGAN, K., STOKES, A.N. & WELSH, M.C. 1988 Resonant sound caused by flow past two plates in tandem in a duct. *J. Fluid Mech.* **192**, 455–484.

TAM, C.K.W. 1976 The acoustic modes of a two-dimensional rectangular cavity. *J. Sound Vib.* **49**, 353–364.

TAM, C.K.W. & BLOCK, P.J.W. 1978 On the tones and pressure oscillations induced by flow over rectangular cavities. *J. Fluid Mech.* **89**, 373–399.

TAM, C.K.W. & NORUM, T.D. 1992 Impingement tones of large aspect ratio supersonic rectangular jets. *AIAA J.* **30**, 304–311.

TAIRA, K., BRUNTON, S.L., DAWSON, S., ROWLEY, C.W., COLONIUS, T., MCKEON, B.J., SCHMIDT, O.T., GORDEYEV, S., THEOFILIS, V. & UKEILEY, L.S. 2017 Modal analysis of fluid flows: an overview. *AIAA J.* **55**, 4013–4041.

THEOFILIS, V. 2011 Global linear instability. *Annu. Rev. Fluid Mech.* **43**, 319–352.

TONON, D., GOLLIARD, J., HIRSCHBERG, A. & ZIADA, S. 2011 Aeroacoustics of pipe systems with closed branches. *Intl J. Aeroacoust.* **10**, 201–276.

TUERKE, F., SCIAMARELLA, D., PASTUR, L.R., LUSSEYRAN, F. & ARTANA, G. 2015 Frequency-selection mechanism in incompressible open-cavity flows via reflected instability waves. *Phys. Rev.* E **91**, 013005.

WANG, P., DENG, Y. & LIU, Y. 2018 Vortex-excited acoustic resonance in channel with coaxial side-branches: vortex dynamics and aeroacoustic energy transfer. *Phys. Fluids* **30**, 125104.

YAMOUNI, S., SIPP, D. & JACQUIN, L. 2013 Interaction between feedback aeroacoustic and acoustic resonance mechanisms in a cavity flow: a global stability analysis. *J. Fluid Mech.* **717**, 134–165.

ZIADA, S. & SHINE, S. 1992 Self-excited resonances of two side branche in close proximity. *J. Fluids Struct.* **6**, 583–601.